# Measurement of the absolute differential cross section for *np* elastic scattering at 194 MeV

M. Sarsour,[1,*] T. Peterson,[1,†] M. Planinic,[1,‡] S. E. Vigdor,[1] C. Allgower,[1] B. Bergenwall,[2] J. Blomgren,[2] T. Hossbach,[1] W. W. Jacobs,[1] C. Johansson,[2] J. Klug,[2] A. V. Klyachko,[1] P. Nadel-Turonski,[2,§] L. Nilsson,[2] N. Olsson,[2] S. Pomp,[2] J. Rapaport,[3] T. Rinckel,[1] E. J. Stephenson,[1] U. Tippawan,[2,4] S. W. Wissink,[1] and Y. Zhou[1]

[1]*Indiana University Cyclotron Facility, Indiana University, Bloomington, Indiana 47401, USA*

[2]*Uppsala University, Uppsala, Sweden*

[3]*Ohio University, Athens, Ohio 45701, USA*

[4]*Chiang Mai University, Chiang Mai, Thailand*

(Received 15 February 2006; published 25 October 2006)

A tagged medium-energy neutron beam was used in a precise measurement of the absolute differential cross section for *np* backscattering. The results resolve significant discrepancies within the *np* database concerning the angular dependence in this regime. The experiment has determined the absolute normalization with ±1.5% uncertainty, suitable to verify constraints of supposedly comparable precision that arise from the rest of the database in partial wave analyses. The analysis procedures, especially those associated with the evaluation of systematic errors in the experiment, are described in detail so that systematic uncertainties may be included in a reasonable way in subsequent partial wave analysis fits incorporating the present results.

DOI: 10.1103/PhysRevC.74.044003 PACS number(s): 13.75.Cs, 21.30.−x, 25.10.+s

## I. INTRODUCTION

Theoretical treatments and applications of the nucleon-nucleon (*NN*) force at low and intermediate energies have progressed considerably in sophistication through the past decade. Partial wave analyses and potential model fits to the *NN* scattering database have incorporated explicit allowance for breaking of isospin ($I$) symmetry, e.g., by removing constraints that previously required equal $I = 1$ phase shifts for the *pp* and *np* systems, and have been used to constrain the pion-nucleon-nucleon coupling constant [1]. Effective field theory approaches [2] have become competitive with more traditional meson-exchange models of the interaction, in terms of the quality of fit provided to the database and the number of adjustable parameters employed, while holding out the promise of providing internally consistent two- and three-nucleon forces from the same theory. Striking success has been achieved in *ab initio* calculations of the structure of light nuclei [3] by combining phenomenological three-nucleon forces with *NN* interactions taken without modification from fits to the *NN* scattering database. An important aspect in these advances has been the approach toward consensus on which measurements should be included in an *NN* database to which conventional $\chi^2$ optimization techniques can be sensibly applied. The rejection of specific, allegedly flawed, experiments from the database has not been without controversy. In the present article, we report detailed results from a new *np* scattering experiment addressing one of the most prominent of these controversies.

Discrepancies among different experiments have led to a drastic pruning of cross section measurements for intermediate-energy *np* scattering. For example, the partial wave analysis (PWA) of the *np* database carried out with the code SAID [4] rejects more than 40% of all measured cross sections in the range 100–300 MeV in neutron laboratory kinetic energy. The rejected fraction is even larger in the Nijmegen PWA [5,6], especially so for scattering at center-of-mass angles beyond 90°. The rejected data include nearly all of the most recent experiments carried out by groups at Uppsala [7] and Freiburg [8,9]. The problems are illustrated in Fig. 1 by the comparison of data from these two groups with earlier Los Alamos measurements [10] that dominate the medium-energy back-angle cross section data retained in the database. Clear differences among these data sets are seen in the shape of the angular distribution. Other differences, reflecting the general experimental difficulty in determining the absolute scale for neutron-induced cross sections, are masked in the figure by renormalization factors that were applied in the partial wave analyses. Removal of the Uppsala and Freiburg data, which exhibit fairly similar angular dependences, begs the question of whether the $\chi^2$ criterion used to reject them [4–6,11] may subtly bias the PWA results toward agreement with older measurements that might have had their own unrecognized systematic errors.

The *np* back-angle cross section discrepancies have been highlighted in debates concerning the value and extraction methods for the charged $\pi NN$ coupling constant $f_c^2$ (in the notation of pseudovector formulations of the interaction, or equivalently $g^2_{\pi^\pm}/4\pi$ in pseudoscalar formulations) [12,13]. *np* scattering PWAs appear to determine this basic parameter of the *NN* force well: e.g., the Nijmegen analysis [5] yields $f_c^2 = 0.0748 \pm 0.0003$ (equivalent to $g^2_{\pi^\pm}/4\pi = 13.54 \pm 0.05$), and the authors claim that the constraints are imposed by the entire database, with no particularly enhanced sensitivity to any specific observable [5]. In contrast, Ericson *et al.* have extracted a significantly higher coupling constant, consistent

*Present address: Dept. of Physics, Texas A & M University, College Station, TX 77843, USA.

†Present address: Dept. of Radiology and Radiological Sciences, Vanderbilt University, Nashville, TN 37235, USA.

‡Present address: Dept. of Physics, University of Zagreb, Zagreb, Croatia.

§Present address: Dept. of Physics, George Washington University, Washington, DC 20052, USA.

 

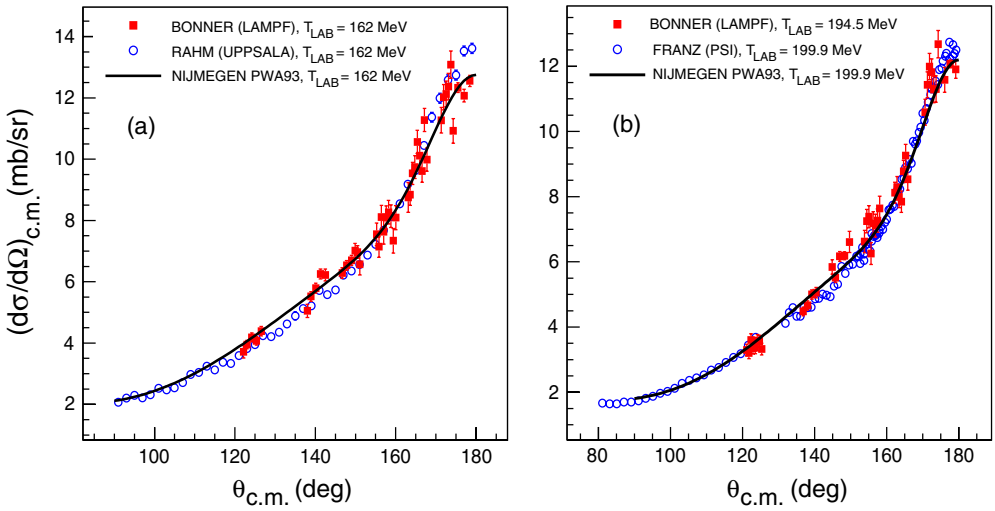


FIG. 1. (Color) Comparison of previous *np* scattering differential cross section measurements (a) from Uppsala [7] and Los Alamos [10] and (b) from PSI [9] and Los Alamos [10] near 200 MeV. The Los Alamos data in each case are represented by solid squares and the other data by open circles. The experimental results are compared to the Nijmegen PWA93 [5] partial wave analysis solution evaluated at appropriate energies. The Los Alamos data were renormalized by factors of 1.092 in (a) and 1.078 in (b) to bring them into agreement with the PWA. The relative cross sections reported in [9] were similarly normalized here, while the reported absolute cross section scale for the Uppsala data was retained.

with older "textbook" values ($g_\pi^2/4\pi \approx 14.4$), by applying controversial pole extrapolation techniques to the Uppsala back-angle *np* scattering cross sections alone [12]. While much debate has centered on the rigor of the pole extrapolation method [13–15], it is clear that the discrepancy in coupling constant values arises in large part [16] from the cross section discrepancies between the Uppsala measurements and the "accepted" database. An experimental resolution of these discrepancies is highly desirable, especially if a new experiment can also pin down the absolute cross section scale. Bugg and Machleidt have pointed out [11] that the largest uncertainty in their determination of $f_c^2$ is associated with the normalization of *np* differential cross sections, which are often allowed to float from the claimed normalization in individual experiments by 10% or more in PWAs. In contrast, the Nijmegen group claims [6] that, despite sizable normalization uncertainties in existing elastic scattering data, precise total cross section measurements fix the *np* absolute cross section scale to $\pm 0.5\%$ accuracy. This claim could also be checked by a new experiment that provides good experimental precision on absolute differential cross sections.

In the present article we report detailed results from such a new experiment, designed to resolve these *np* back-angle cross section discrepancies. The experiment employed techniques completely independent of those used in other medium-energy measurements, in order to provide tight control over systematic errors. A tagged neutron beam [17] centered around 194 MeV kinetic energy bombarded carefully matched, large-volume $CH_2$ and C targets, which permitted accurate subtraction of backgrounds from quasifree scattering and other sources. The bombarding energy range was chosen to match approximately that used in earlier high-precision *np* scattering polarization measurements from the Indiana University Cyclotron Facility (IUCF) [18–20]. Recoil protons from *np* scattering were identified in a detector array of sufficient angular coverage to measure the differential cross section at all c.m. angles beyond 90° simultaneously.

The tagging allows accurate determination of the absolute scattering probability for the analyzed subset of all neutrons incident on a secondary target, but it also offers a host of other, less obvious, advantages important to a precise experiment: (1) accurate relative normalization of data taken with $CH_2$ vs C targets; (2) event-by-event determination of neutron energy, impact point, and incidence angle on the secondary target, with the latter measurement being especially important for cross section measurements very near 180° c.m. scattering angle; (3) three-dimensional location of background sources displaced from the secondary target [17]; (4) precise measurement of the detector acceptance for *np* scattering events; and (5) methods to tag *np* scattering event subsamples that should yield identical cross section results but different sensitivity to various sources of systematic error. The tagging was thus essential to the entire approach of the experiment; no *extra* work was required to extract *absolute* cross sections and thereby to provide an important calibration standard for medium-energy neutron-induced reactions.

The basic results of this experiment have recently been reported briefly [21]. In the present article we provide more detail on the comparison of results to PWAs, on the data analysis procedures, and on the evaluation and characterization of systematic uncertainties. Such details are important for resolving the sort of discrepancies that have plagued the *np* database. Partial wave analyses should, in principle, incorporate experimental systematic as well as statistical errors in optimizing fits to data from a wide variety of experiments. To do so, they must have access to clear delineations of which errors affect only the overall normalization, which have angle dependence, and, in the latter case, what the degree

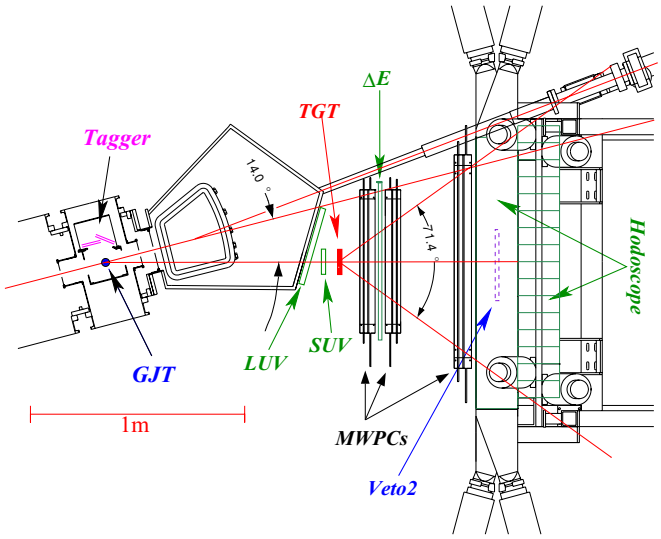


FIG. 2. (Color online) Top view of the *np* scattering experiment setup.

of correlation is among errors at different angles. Overall systematic uncertainties in the absolute cross sections reported here average $\pm 1.6\%$, with a slight angle dependence detailed herein. Statistical uncertainties in the measurements are in the range $\pm(1-3)\%$ in each of 15 angle bins.

## II. DETAILS OF THE EXPERIMENT

The experiment was carried out in the IUCF Cooler Ring [22], with apparatus (see Fig. 2) installed in a ring section where the primary stored proton beam was bent by 6°. A primary electron-cooled unpolarized proton beam of 202.5 MeV kinetic energy and typical circulating current of 1–2 mA was stored in the ring. Neutrons of 185–197 MeV were produced via the charge-exchange reaction $p + d \rightarrow n + 2p$ when the proton beam passed through a windowless internal deuterium gas jet target (GJT) of typical thickness $\approx 3 \times 10^{15}$ atoms/cm$^2$. The ultrathin target permitted detection of the two associated low-energy recoil protons from the production reaction in double-sided silicon strip detectors (DSSDs) comprising the "tagger." Measurements of energy, arrival time, and two-dimensional position for both recoil protons in the tagger, when combined with the precise knowledge of cooled primary proton beam direction and energy, allowed four-momentum determination for each tagged neutron on an event-by-event basis. During the measurement periods, the stored proton beam was operated in "coasting" mode, with rf bunching turned off to minimize the ratio of accidental to real two-proton coincidences in the tagger. The proton beam energy was then maintained by velocity matching (induced naturally by mutual electromagnetic interactions) to the collinear electron beam in the beam cooling section of the ring.

Details of the layout, design, and performance of the tagger detectors and of the forward detector array used to view *np* scattering events from the secondary target are provided in Ref. [17]. Here, we summarize the salient features briefly. The tagger included an array of four $6.4 \times 6.4$ cm$^2$ DSSDs with 480 $\mu$m readout pitch in two orthogonal $(x', y')$ directions, each followed by a silicon pad ("backing") detector (BD) of the same area. The DSSDs were positioned about 10 cm away from the center of the gas jet production target. Each DSSD had 128 $x'$ and 128 $y'$ readout channels. Readout was accomplished with front-end application-specific integrated circuits (ASICs) that provided both timing and energy information [17]. The timing signals provided to external electronics consisted of the logical OR over groups of 32 adjacent channels of leading-edge discriminator signals based on fast shaped and amplified analog signals generated in the ASICs. The timing signals available from $4x' \times 4y'$ logical pixels for each DSSD permitted operation of the tagger in a self-triggering mode, where the time-consuming digitization of slow pulse height signals from all 1024 DSSD channels could be initiated by logic based solely on the tagger hit pattern, as reconstructed from the fast timing signals. This self-triggering was critical to the determination of precise absolute cross sections, because it allowed acquisition of data to count directly the flux of tagged neutrons that did not interact in the secondary target or in any of the forward detectors.

Only recoil protons that stopped either in the DSSDs ($E_p \lesssim 7$ MeV) or BDs ($E_p \lesssim 11$ MeV) were considered in the data analysis, because for these the tagger provided a measurement of total kinetic energy with good resolution. By combining these energy measurements with position measurements for both recoil protons, we were able to determine the energy and angle of each tagged neutron, within their broad distributions, with respective resolutions of $\sigma_E \approx 60$ keV and $\sigma_{\text{angle}} \approx 2$ mrad. As part of this determination, we reconstructed the longitudinal origin ($z_{\text{vertex}}$) of each produced neutron within the extended GJT density profile with a resolution of $\approx 2$ mm, by comparing neutron momentum magnitudes inferred by applying energy conservation (independent of vertex position) vs vector momentum conservation (dependent on vertex position) to the tagger information for the two recoil protons. Similar resolution was obtained for the transverse coordinates at which each tagged neutron impinged upon a secondary scattering target (TGT in Fig. 2) positioned 1.1 m downstream of the GJT.

Two solid secondary targets were used during the production running: a $20 \times 20 \times 2.5$ cm$^3$ slab of ultra-high-molecular-weight polyethylene ($CH_2$) containing $1.99 \times 10^{23}$ hydrogen atoms/cm$^2$ and a graphite target of known density machined to have identical transverse dimensions and the same number of carbon atoms per unit area. Each target thickness was determined to $\pm 0.4\%$ by weighing. Data were collected in 18-h cycles, comprising 6 h of running with the $CH_2$ target, followed by 6 h with C, and 6 h more with $CH_2$. The frequent interchange of the targets facilitated accurate background subtractions. Both targets intercepted neutrons over an approximate production angle range of $14° \pm 5°$, and cuts were generally placed on the tagger information during data analysis to confine attention to tagged neutrons that would hit the secondary target. Such tagged neutrons were produced at a typical rate of $\sim 200\,\text{s}^{-1}$, leading to typical free *np* backscattering (angle-integrated) rates $\sim 1\,\text{s}^{-1}$ from the $CH_2$ target.

Protons emerging from the secondary target were detected in a forward array of plastic scintillators for triggering and

energy information, and a set of (three-plane) multiwire proportional chambers (MWPCs) for tracking, as indicated in Fig. 2. The plastic scintillators included large upstream veto (LUV) and small upstream veto (SUV) counters to reject charged particles produced upstream of the secondary target. The ΔE scintillator was separated from the secondary target by a MWPC to permit easy discrimination against *np* scattering events initiated in that scintillator. The rear hodoscope comprised 20 plastic scintillator bars [23] of sufficient thickness (20 cm) to stop 200 MeV protons and give 15%–20% detection efficiency for 100–200 MeV neutrons. All forward detectors were rectangular in transverse profile, with the rear MWPC and hodoscope spanning a considerably larger vertical than horizontal acceptance. The entire forward array provided essentially 100% (>50%) geometric acceptance for *np* scattering events initiated at the $CH_2$ target for angles $\theta_{\text{c.m.}} \gtrsim 130^\circ$ ($\theta_{\text{c.m.}} \gtrsim 90^\circ$). For c.m. angles forward of 90° the large size and significant neutron detection efficiency of the hodoscope provided a small efficiency for detecting forward-scattered neutrons in coincidence with larger-angle protons that fired at least the first two MWPCs.

The tagger and forward detector array were designed to facilitate a kinematically complete double-scattering experiment with a first target giving negligible energy loss. With the same apparatus, a similar measurement of *pp* scattering was possible simultaneously. For this purpose one could use the tagger to detect a single large-angle recoil deuteron instead of two recoil protons to tag a secondary proton beam via *pd* elastic scattering in the GJT. By requiring a coincidence between a single hit in the tagger and a signal from the small upstream veto scintillator (SUV in Fig. 2), we could define a secondary proton beam of transverse dimensions very similar to those of the tagged neutron beam. Another scintillator (Veto2) placed just in front of the rear hodoscope allowed us to distinguish, at trigger level, between protons from *pd* elastic scattering that traversed the forward array without further nuclear interactions and protons that scattered out of this secondary beam in material following SUV. In the present article, we discuss only the former group, as their yield provides an accurate relative normalization of runs taken with the $CH_2$ vs C targets.

The triggered events of interest for the present analysis were recorded in four mutually exclusive event streams, three for tagged neutron candidates (consistent with two distinct tagger hits and no accompanying signals from LUV or SUV) and one for tagged proton candidates (consistent with a single tagger hit in prompt coincidence with both LUV and SUV). The trigger logic defined these event streams as follows: (1) tagged neutrons with no rear hodoscope coincidence, providing a prescaled (by a factor of 20) sample for neutron flux monitoring; (2) *np* scattering candidates for which a tagged neutron was in coincidence with signals from both the $\Delta E$ scintillator and the rear hodoscope; (3) tagged neutrons in coincidence with the hodoscope but *not* with the $\Delta E$ scintillator, a sample used for evaluating the neutron detection efficiency of the hodoscope [17]; and (4) tagged protons in coincidence with both the $\Delta E$ and Veto2 scintillators, providing a prescaled (by a factor of 10) sample including *pd* elastic scattering events from the GJT, used to cross-normalize C and $CH_2$ secondary target runs. The total flux of tagged neutrons intercepting the secondary target was determined from a sum over event streams (1) + (2) + (3), while comparative analyses of the three streams facilitated crosschecks to calibrate the system [17] and aid understanding of potential systematic errors.

## III. DATA ANALYSIS

### A. Cuts and conditions on tagged neutron beam properties

The general philosophy of the data analysis was to define properties of the tagged neutron beam by identical cuts applied to event streams (1)–(3), so that associated systematic uncertainties would cancel in the yield ratios from which the absolute *np* scattering cross section is extracted. Among these common cuts, described in more detail below, were ones to remove BD noise contributions correlated among the four quadrants of the tagger, to identify the recoil particles detected in the tagger, and to divide the tagged neutron events into subsamples for subsequent analysis. Additional cuts defined a fiducial range for the tagged neutron's predicted transverse coordinates at the secondary target ($|x_{\text{tag}}| <$ 9.5 cm and $|y_{\text{tag}}| < 9.5$ cm) and selected prompt tagger two-particle coincidences ($|t_{p1} - t_{p2} - 30\,\text{ns}| \leqslant 70$ ns, where $t_{p1}(t_{p2})$ is the arrival time of the recoil proton with the larger (smaller) DSSD energy deposition). Software cuts applied to event stream (2) alone to identify free *np* scattering events were kept to a minimum to avoid complicated systematic errors. We relied instead on the accuracy of the background subtractions, which could be verified to high precision. Before application of cuts, additional MWPC requirements were added in software to amplify the hardware definitions of the various triggers. Thus, at least one hit in the $x$ plane and at least one hit in the $y$ plane were required for each of the three MWPCs for events from stream 2.

#### *1. Particle identification*

The correlation of DSSD vs BD energy depositions was used to select two basic event classes for analysis of each of the three tagged neutron event streams: (a) "2-stop" events, where both protons associated with the neutron stopped inside the DSSD (either the same or different quadrants of the tagger); and (b) "1-punch" events, where one of the protons stopped inside a DSSD and the other punched through to the BD in a different quadrant and stopped there. These two classes, as discussed further below, differ significantly in neutron energy ($E_n$) and position ($x_{\text{tag}}$) profiles, allowing an important crosscheck on the accuracy of the tagging technique by comparing *np* cross sections extracted independently from each class. The 2-stop events were further subdivided according to whether the higher of the two recoil proton DSSD energy depositions ($E_{p1}$) was below or above 5.0 MeV. Protons with $E_{p1} > 5.0$ MeV range out near the exit of the DSSD, and hence possibly in dead layers at the back of the DSSD or front of the BD, making this event class subject to somewhat greater ambiguity regarding complete recoil proton energy reconstruction and accuracy of the predicted $x_{\text{tag}}$ value for the

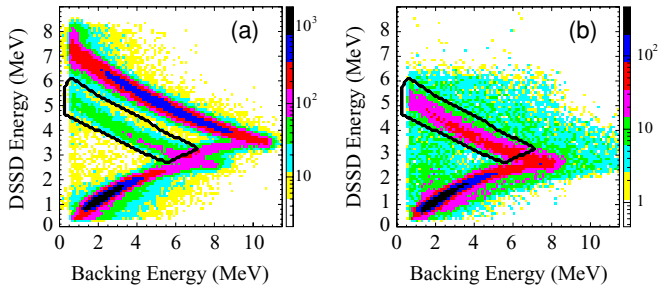


FIG. 3. (Color online) Particle identification plot for one DSSD-BD combination for (a) tagged proton candidates and (b) tagged neutron candidates. The two-dimensional gate used as part of the selection criteria for 1-punch tagged neutron events is shown in panel (b), and again in panel (a), where its location can be gauged with respect to both recoil deuterons and recoil protons that punch through the backing detector.

tagged neutron. Events where both protons punched through to the BDs, or where either punched through the BD itself, were not included in the analysis because they corresponded to $E_n$ below the range of interest.

Figure 3 shows raw spectra for both tagged neutron candidates [event stream 1 in panel (b)] and tagged proton candidates [event stream 4 in panel (a)] of the energy deposited in a typical DSSD quadrant vs that in the companion BD when the latter is nonzero. The tagged proton events exhibit clear recoil proton (lower) and deuteron (upper) particle identification loci, while only the proton locus remains for tagged neutron events. The loci bend backward when the detected particle begins to punch through the BD. The two-dimensional gate (dark boundary) shown in each panel was used to select recoil protons that enter and stop inside the BD, e.g., to identify the 1-punch tagged neutron events. Note that the most intense region along the proton locus, corresponding to deuteron breakup events with an energetic large-angle proton, is thereby eliminated. So are events lying off the proton locus, where the backing detector response may be corrupted by noise or pileup.

Figure 4 shows the reconstructed $E_n$ and $x_{\mathrm{tag}}$ distributions for the tagged neutrons in the 2-stop (for all values of $E_{p1}$) vs 1-punch samples. While the two samples yield overlapping distributions, it is clear that the 1-punch events correspond on average to lower-energy neutrons at larger production angles (preferentially populating the beam-right side of the secondary target).

### 2. *Correlated noise in the BD*

Special care was taken in the definitions of 1-punch and 2-stop events to minimize effects of substantial detector noise picked up by the large-capacitance BDs. An important source of this noise was discovered to arise from the initiation of pulse height information readout on the adjacent DSSD front-end electronics [17]. The induced noise was strongly correlated among the four BDs, as illustrated in Fig. 5. This figure reveals two uncorrelated bands parallel to the $x$ and $y$ axes, due to 1-punch events in one of the quadrants and low pulse height noise in the other (the pedestals for each BD appear in ADC channel ≈10). But one also observes a strong diagonal band indicative of noise correlations between the two quadrants.

Since the noise correlation pattern extends beyond a reasonable software threshold, it was necessary to use a two-dimensional gate, such as that shown in Fig. 5, to bound the noise correlation region. Candidates for valid 1-punch events were then required to: (1) surpass a threshold ADC channel (≈15) on at least one BD; (2) fall outside the noise correlation gates for all BD pairs; (3) not surpass the BD noise peak (ADC ≈70) in more than one BD; and (4) fall within the PID gate in Fig. 3 for the appropriate quadrant. These conditions and the complementary ones required for 2-stop events reduced the flux of tagged neutrons considered for subsequent analysis by removing events with BD pulse height ambiguities, but because they were applied equally to all

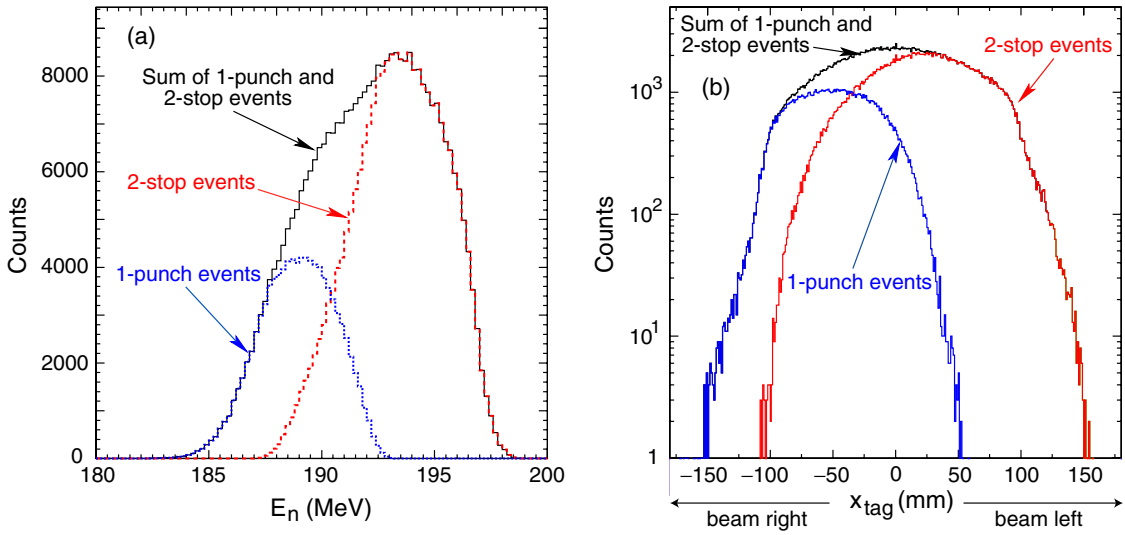


FIG. 4. (Color online) The reconstructed energy (a) and horizontal transverse coordinate (b) of tagged neutrons at the secondary target for 1-punch events, 2-stop events, and their sum (solid black line).

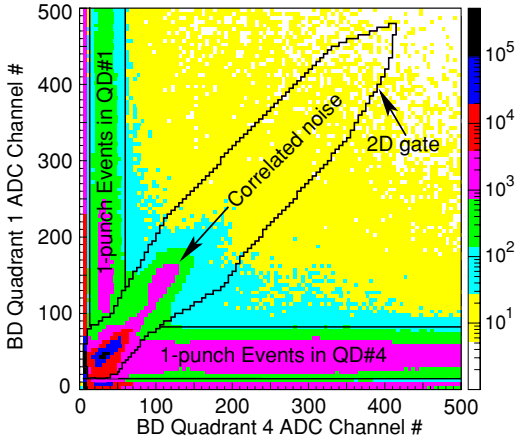


FIG. 5. (Color online) The ADC outputs of two BDs plotted against one another, revealing regions of 1-punch tagged neutron events, but also a region dominated by correlated noise in both quadrants. Events along the $x$ and $y$ axes, where one BD signal falls in the pedestal region, are also mostly valid 1-punch events.

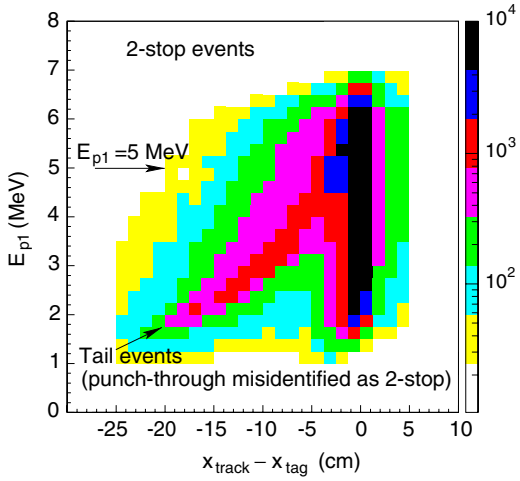


FIG. 6. (Color online) The correlation for apparent 2-stop *np* scattering candidates between the higher of the DSSD energy depositions for the two recoil protons in the tagger and the difference in predicted $x$ coordinates at the secondary target from neutron tagging vs forward proton ray-tracing. The long correlated tail contains corrupted punch-through events for which electronic loss of backing detector energy information has led to misidentification of the event and large systematic errors in the tagging.

tagged neutron event streams they did not introduce systematic errors in the *np* cross section extraction.

### B. Corrupted events subtraction

An event misidentification mechanism discovered during the data analysis was attributed to an electronics malfunction in the gating or clearing circuit for the electronics module that was used to digitize the pulse height information for all four BDs. The effect of the malfunction was to zero out valid BD energy signals for a randomly selected fraction of punch-through events. The effect was seen clearly, for example, in the *pd* elastic scattering events in stream 4, where a software gate placed on the two-body kinematic correlation between recoil deuteron DSSD energy deposition and forward proton angle could be used to select events in which the deuteron must have stopped in the BD. Roughly 3/4 of these events showed the anticipated BD pulse height, but 1/4 had $E_{\mathrm{BD}} = 0$. In the case of tagged neutrons, the corrupted events were misidentified as 2-stop events and gave systematically incorrect predictions of the tagged neutron trajectory, because some recoil proton energy was lost. However, the availability of full information for the surviving punch-through samples allowed us to emulate the effect and subtract the corrupted events accurately.

The corrupted events were easily distinguished in event stream 2 by using the MWPC tracking information. Figure 6 shows the correlation for event stream 2 between $E_{p1}$ in the tagger and $x_{\mathrm{track}} - x_{\mathrm{tag}}$, where $x_{\mathrm{track}}$ denotes the transverse coordinate of the detected proton from *np* scattering at the secondary target, as reconstructed from the MWPC hits. The majority of events have $x_{\mathrm{track}} - x_{\mathrm{tag}} \approx 0$, independent of $E_{p1}$, as expected when both the tagging and tracking are accurate. The corrupted events populate the "tail" to the left of the most intense band, with $x_{\mathrm{tag}}$ exceeding $x_{\mathrm{track}}$ by an amount that is strongly correlated with the recoil proton energy deposition in the DSSD: the lower $E_{p1}$, the larger is the lost $E_{\mathrm{BD}}$ and the consequent error in $x_{\mathrm{tag}}$. While the corrupted events could be eliminated from event stream 2 by a software gate within Fig. 6, they could not have been similarly eliminated from event streams 1 and 3, where there was no forward proton to track. Hence, it was essential to find a way to subtract these corrupted events reliably and consistently from all three tagged neutron event streams.

The corrupted events were simulated using all recorded punch-through events that survived with their BD energy information intact by reanalyzing these events after artificially setting $E_{\mathrm{BD}} = 0$ in the software before tagging reconstruction. The distribution shapes of the tail events in Fig. 6 with respect to all variables were accurately reproduced when this simulation was based on *all* events in Fig. 3(b), both inside and outside the two-dimensional gate drawn, and also including events where *both* recoil protons punched through their DSSDs. To determine the fraction of these punch-through events that was affected by the electronics malfunction, we relied on a comparison of the subsamples of our simulated events and of the apparent 2-stop events that had valid BD timing information despite having $E_{\mathrm{BD}} = 0$. Because the BD noise problems necessitated high thresholds to generate timing signals, these subsamples populate mostly the far tail in Fig. 6, corresponding to $E_{p1} \lesssim 3.5$ MeV (thus, to relatively large BD analog signals). The corrupted fraction of punch-through events was in this way determined independently for each of the three tagged neutron event streams and found to be identical for the three, within the statistical precision (typically $\approx$1%) available in matching simulated and recorded corrupted event subsamples. The fraction varied slightly with time during the production run, but averaged 23%. The success of this simulation and the persistence of the corrupted fraction across (both tagged neutron and tagged proton) event streams provide strong support for our assumption that the malfunction

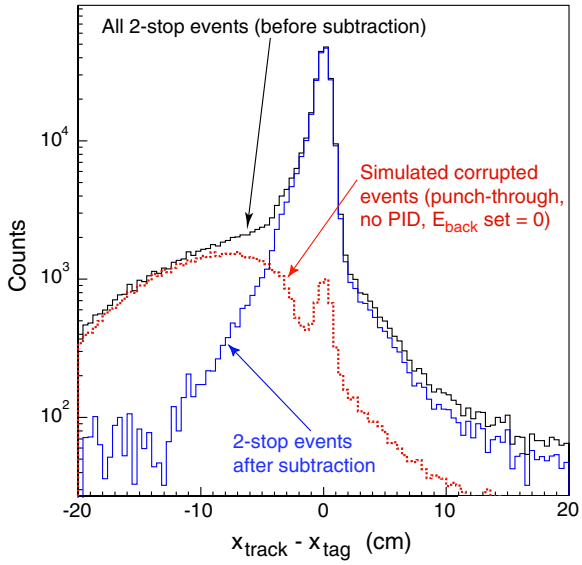


FIG. 7. (Color online) The subtraction of the simulated corrupted events removes the tail from the 2-stop event sample. The simulated spectrum has been normalized by matching to the 2-stop subsample characterized by backing detector information with valid times but zero energy.

affected a random sample of punch-through events. Because the fractional loss of 1-punch events to this corruption was independent of event stream, there was no residual systematic effect on the extracted 1-punch cross sections, but rather only a slight loss of statistical precision.

Figure 7 shows a comparison of the $x_{\rm track} - x_{\rm tag}$ spectrum for all 2-stop events in stream 2 with the simulated corrupted sample, normalized as described above via the subsample with valid BD timing signals. The subtraction eliminates essentially completely the corrupted events with $E_{p1} \lesssim 5.0$ MeV, or $x_{\rm track} - x_{\rm tag} \lesssim -5$ cm, leaving a reasonably symmetric small background (discussed further in Sec. V A5) at $|x_{\rm track} - x_{\rm tag}| > 5$ cm. We therefore assume that the subtraction is similarly successful for event streams 1 and 3, where we have no tracking information to compare, and associate a systematic error for the subtraction (see Sec. V B2) that reflects only the uncertainty in the normalization scheme for the simulated corrupted events.

For $E_{p1} > 5.0$ MeV, there is a remaining tail of small extent in the subtracted $x_{\rm track} - x_{\rm tag}$ spectrum in Fig. 7 that arises not from the electronics malfunction but rather from recoil protons that barely punch through the DSSD, while depositing insufficient energy in the BD to be distinguished from noise. Because of these events, we have separately analyzed the 2-stop samples with $E_{p1} \leqslant 5.0$ MeV and $E_{p1} > 5.0$ MeV. For the latter sample, after subtracting simulated corrupted events, we used a two-dimensional software gate on Fig. 6 to eliminate events in stream 2 that had potentially distorted $x_{\rm tag}$ information, thereby rejecting 18% of 2-stop $E_{p1} > 5.0$ MeV events (as opposed to the 23% of *all* 2-stop events in stream 2 that were affected by the corruption). The yields of 2-stop $E_{p1} > 5.0$ MeV events in streams 1 and 3 were then scaled down by the same 18% to remove the remaining events of questionable 2-stop pedigree.

The small peak at $x_{\rm track} - x_{\rm tag} \approx 0$ in the simulated background in Fig. 7 indicates that a small fraction of the punch-through event sample used in the simulation really corresponds to true 2-stop events that were misidentified by virtue of BD noise that evaded the noise cuts discussed in the preceding subsection. Subtracting this small fraction of valid 2-stop events along with the simulated corrupted events has the effect of reducing the 2-stop tagged neutron yield by ≈3% in all three event streams, with no significant consequence for the absolute *np* cross sections extracted from the 2-stop sample.

### C. Background subtraction

The background events for this experiment came mostly from *np* quasifree scattering off carbon nuclei in the $CH_2$ target. However, there were also some prominent sources displaced from the secondary target, including: (1) protons coming directly from the gas jet production target, or from the exit flange on the Cooler beam 6° magnet chamber (see Fig. 2), that evaded the veto scintillators because of either their imperfect coverage or their electronic inefficiencies; (2) *np* scattering events induced either on scintillator edges or on the Lucite light guide for the SUV, yielding pulse heights below that veto detector's threshold; and (3) quasifree *np* scattering induced on the vertically narrow (but longitudinally thick) aluminum frame used to support the secondary target. By frequently interchanging the $CH_2$ target with a graphite target closely matched in transverse dimensions and in areal density of carbon nuclei, we were able to subtract the backgrounds from all sources simultaneously. The relative normalization of the $CH_2$ and C runs was determined from the *pd* elastic scattering yield from the GJT, as recorded in event stream 4 [17]. The background subtraction was determined to be sufficiently reliable that we could avoid imposing many kinematic cuts, with potentially significant systematic ambiguities, to define free *np* scattering events.

The accuracy of the background subtraction can be judged, for example, from Fig. 8, which presents $CH_2$ and C spectra, and their difference, with respect to $y_{\rm tag}$ (the vertical impact position of the neutron on the secondary target, as reconstructed from the tagger) and $\Delta E$ scintillator pulse height within a narrow *np* scattering angle range. These two particular variables have been chosen for display in the figure because the $CH_2$ spectra show prominent background features associated both with quasifree scattering (the long high pulse height tail in $\Delta E$) and with other sources (the $y_{\rm tag} = -11$ cm peak from the aluminum support frame). Both sources are precisely eliminated by the background subtraction. Indeed, upper limits on the surviving remnants of these features allow us (as described in Sec. V B1) to reduce the systematic uncertainty for the background subtraction even below the level given by the precision of the measured C/$CH_2$ target thickness ratio (±0.6%). Comparison of the $y_{\rm tag}$ spectra for C and $CH_2$ in Fig. 8 also reveals another localized non-target source, near $y_{\rm tag} = 0$, that is removed by the subtraction. This appears to be localized horizontally as well, to a region near the beam-left edge of the SUV scintillator, and might reflect scattering from a small damaged region of that scintillator with reduced light collection and veto efficiency.

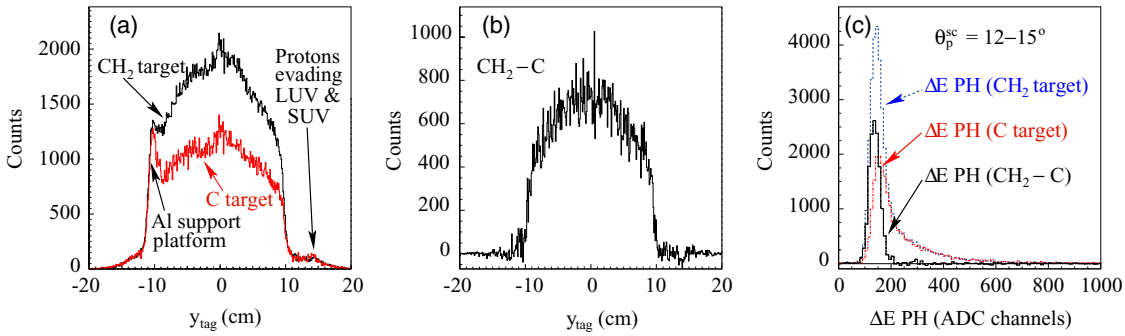


FIG. 8. (Color) Distribution of *np* scattering event candidates with respect to $y_{tag}$ and to $\Delta E$ scintillator pulse height for the $CH_2$ and C targets separately and for the difference between them.

### D. Free scattering cuts

Software conditions imposed only on event stream 2 to distinguish free scattering from background events have the potential to remove free scattering yield in sometimes subtle ways. They were thus used in the analysis only when they could substantially reduce the statistical uncertainties (i.e., by suppressing background to be subtracted) without introducing significant systematic uncertainties in correcting for the free scattering losses, or when such losses were judged to be inevitable to remove ambiguities in the analysis. The accuracy of the C background subtraction provided a reliable method to judge the extent of any free scattering event removal.

The most effective such cut applied was placed on the correlation of forward proton energy loss in the $\Delta E$ scintillator with the laboratory angle of the proton trajectory. The applied two-dimensional software gate is superimposed on the observed distribution of events following $CH_2$-C subtraction in Fig. 9. This distribution reveals that very few free scattering events were removed by this gate, but it is clear from the long tail seen in the projected unsubtracted spectrum for one angle bin in Fig. 8(c) that a substantial number of quasifree background events, leading to lower-energy outgoing protons, were successfully removed.

In contrast, we did not apply a comparable cut on the energy deposition of the forward proton in the rear hodoscope, where it generally stopped, despite an appreciable difference in the distributions of hodoscope energy between free and quasifree events. The reason for avoiding this cut is illustrated in Fig. 10: the free scattering spectrum revealed by the C subtraction exhibits a quite substantial low-energy reaction tail in addition to the well-defined full-energy peak. An unacceptably large systematic error would have been introduced by the need to correct for loss of these reaction tail events if we had imposed a cut on hodoscope energy to suppress background.

A benign cut imposed for slight background reduction placed an upper threshold on the $\chi^2$ value obtained for a linear track fit to the reconstructed MWPC space points. The $CH_2$-C subtraction indicates that only $(0.2 \pm 0.1)\%$ of free scattering

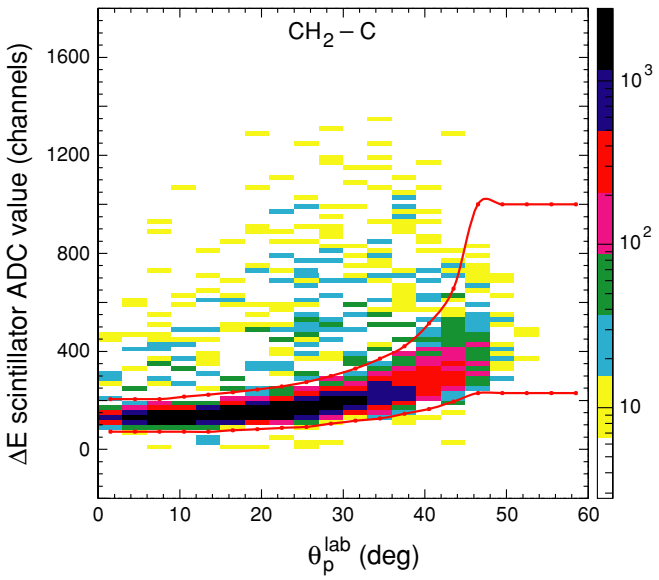


FIG. 9. (Color online) The distribution of *np* scattering candidate events after subtraction of C from $CH_2$ data with respect to $\Delta E$ ADC and proton lab angle. The lines show the boundaries of the gate applied to event stream 2 to select free scattering events.

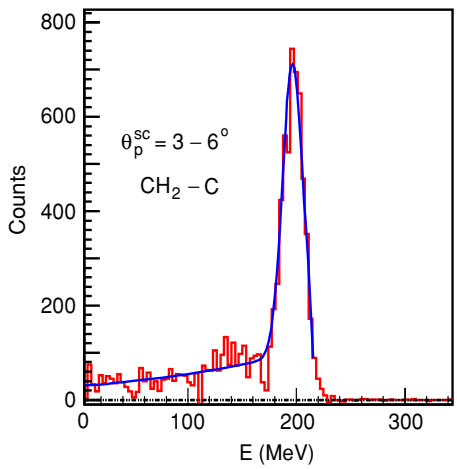


FIG. 10. (Color online) The distribution of *np* free scattering events in the scattering angle bin $\theta_p^{sc} = 3°$–$6°$ with respect to forward proton energy deposition in the rear hodoscope. The curve represents a fit with a Gaussian plus exponential tail. The tail represents valid free scattering events where the proton undergoes a nuclear reaction in the stopping scintillator.

events were removed by this condition. More serious (6.3% of total $CH_2$-C yield), but unavoidable, losses were introduced by cuts confining the tagging and tracking information in event stream 2 to agree within $|x_{\rm track} - x_{\rm tag}| \leqslant 2.5$ cm and $|y_{\rm track} - y_{\rm tag}| \leqslant 2.0$ cm. These limits correspond to $\pm 3\sigma$ of the narrow Gaussian resolution function that dominates these distributions in the $CH_2$-C spectra. Nonetheless, the cut eliminates events in long distribution tails that are affected either by tagging errors or by sequential reactions of the tagged neutron, which introduce serious ambiguities in interpretation. This cut, and its consequence for systematic uncertainties, is discussed further in Sec. V A5.

Finally, it is worth mentioning one additional cut that we chose *not* to impose. The transverse *np* vertex coordinates are, in fact, determined by the tagging and tracking with considerably better resolution than implied by the $\sigma \approx 7$–8 mm value mentioned in the preceding paragraph [17]. This latter value is dominated by the thickness of the secondary target, simply reflecting the uncertainty in precise longitudinal origin of the *np* scattering vertex. Much better information is, in principle, available by locating the vertex in three dimensions at the point of closest approach of the neutron trajectory reconstructed from the tagger and the proton trajectory reconstructed from the MWPCs. Distributions of such reconstructed secondary vertex coordinates [17] permit tagged neutron radiography of the background sources displaced from the $CH_2$ target. However, any cuts to remove such background sources in this manner would be affected by the strong dependence of the reconstructed vertex resolution on the proton scattering angle (vertex information clearly deteriorates as the neutron and proton trajectories approach collinearity). We decided to rely completely on the C subtraction to remove such other sources of background, in order to avoid consequent angle-dependent free scattering event losses.

### E. Acceptance

The lab-frame proton scattering angle $\theta_p^{\rm sc}$ is determined for each analyzed event as the opening angle between the neutron trajectory reconstructed from the tagger and the forward proton trajectory reconstructed from the MWPCs. The geometric acceptance of the forward detector array for *np* scattering events is a function of both $\theta_p^{\rm sc}$ and the coordinates of the scattering vertex at the secondary target. Because the distribution of scattering vertex coordinates, especially of $x_{\rm tag}$ (see Fig. 4), differed among the three analyzed data subsamples (1-punch, 2-stop with $E_{p1} \leqslant 5.0$ MeV, and 2-stop with $E_{p1} > 5.0$ MeV), the acceptance had to be evaluated separately for each subsample. This was done by comparing simulated to measured distributions of events with respect to azimuthal angle $\phi_p^{\rm sc}$ within each $\theta_p^{\rm sc}$ bin, for each data subsample.

The simulations were constrained to reproduce the measured distributions of the longitudinal production vertex coordinate of the neutron within the GJT (common to all three data subsamples) and its transverse coordinates on the secondary target (separately for each subsample). Within these distributions, coordinates were generated randomly for each event, as were also $\theta_p^{\rm sc}$ (in the range 0°–75°) and $\phi_p^{\rm sc}$ (over the full azimuthal range). Generated outgoing proton trajectories were then accepted if they would yield signals above the hodoscope pulse height threshold (required in trigger) and in all three MWPCs (required in the data analysis). Forward detector location parameters were tuned slightly from their measured values to optimize the fit of the simulated to the measured $\phi_p^{\rm sc}$ distributions for all $\theta_p^{\rm sc}$ bins and for 1-punch and 2-stop samples simultaneously.

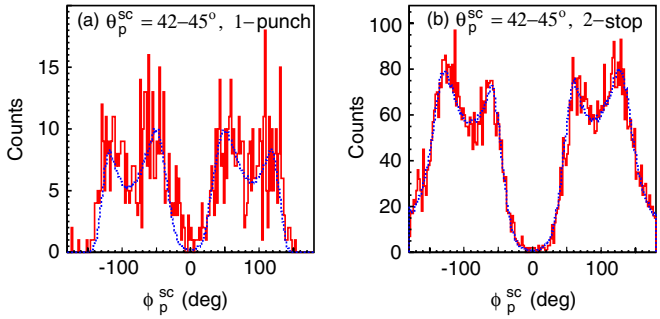


FIG. 11. (Color) Comparison of the measured (solid line with sizable statistical fluctuations) and simulated (dotted line) distributions of free ($CH_2$-C) *np* scattering events in the angle bin $\theta_p^{\rm sc} = 42°$–45° with respect to proton azimuthal scattering angle $\phi_p^{\rm sc}$ for the 1-punch (a) and 2-stop (b) data samples. Forward detector geometry parameters, plus a single overall normalization parameter per angle bin and data sample, were adjusted to optimize the fit simultaneously for all angle bins and both data samples.

The high quality of the fits obtained is illustrated in Fig. 11 for the 1-punch (a) and 2-stop (b, summed over all $E_{p1}$) samples for a single large angle bin, $\theta_p^{\rm sc} = 42°$–45°, where the observed azimuthal distributions display considerable structure. The structure reflects the rectangular shape of the hodoscope and large MWPC, projected onto $\theta - \phi$ space: e.g., the four peaks observed correspond to the four detector corners. The small changes in distribution between the 1-punch and 2-stop samples – e.g., in the relative heights of the peaks and in the extent of the dips near $\phi_p^{\rm sc} = 0°$ (beam-left side) and 180° (beam right) – arise from the shift in $x_{\rm tag}$ profiles seen in Fig. 4. These features are all reproduced very well by the simulations. For $\theta_p^{\rm sc} \leqslant 24°$, the measured and simulated $\phi$ distributions are essentially uniform over $2\pi$, indicating full acceptance. Figure 12 shows the simulated acceptance for the 1-punch data sample as a function of $\theta_p^{\rm sc}$. The 0.2% shortfall from full acceptance near 0° reflects protons incident normally on the small cracks between adjacent hodoscope elements. Results presented in the next section are limited to the angle range for which the acceptance is at least 50%; at larger proton angles the uncertainty in acceptance grows rapidly.

## IV. RESULTS

The absolute differential cross section for *np* backscattering was extracted independently for three data samples – 1-punch, 2-stop with $E_{p1} \leqslant 5$ MeV, and 2-stop with $E_{p1} > 5$ MeV–from

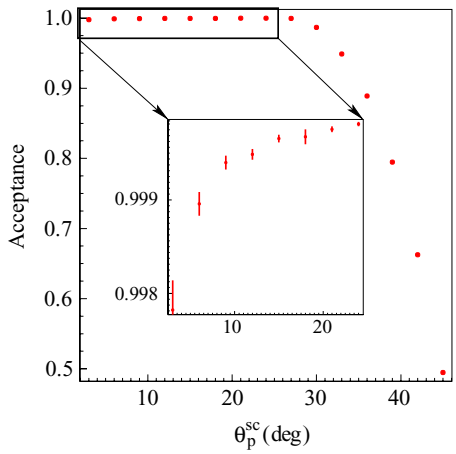


FIG. 12. (Color online) The simulated acceptance of the 1-punch data sample. The inset shows a greatly magnified vertical scale for the most forward proton scattering angles.

the yields of event streams 1, 2, and 3 as follows:

$$\left(\frac{d\sigma}{d\Omega}\right)_{\rm lab} = \frac{N_2(\theta_p^{\rm sc})\prod c_i}{(N_1+N_2+N_3)t_H|d\cos(\theta_p^{\rm sc})|a_\phi(\theta_p^{\rm sc})}, \quad (1)$$

where $N_2(\theta_p^{\rm sc})$ represents the number of free scattering events from stream 2 within a given reconstructed proton angle bin, surviving all relevant cuts and background subtractions; $N_1$, $N_2$, and $N_3$ in the denominator represent analogous tagged neutron yields from the mutually exclusive event streams 1 (corrected for prescaling), 2 (angle-integrated), and 3; the $c_i$ represent small corrections, summarized in Table I with details in Sec. V, for various inefficiencies, tagged neutron losses or backgrounds, software cut and dead time differences among event streams, and resolution smearing; $t_H = (1.988 \pm 0.008) \times 10^{23}$ H atoms/cm$^2$ for the $CH_2$ target; and $a_\phi$ is the azimuthal acceptance determined from simulations for the given angle bin. The data were analyzed in 1 MeV wide slices of reconstructed neutron energy from 185 to 197 MeV and an effective cross section was extracted at the mean neutron energy of $194.0 \pm 0.15$ MeV. For this purpose, a small (always $<1\%$) cross section correction was made for the deviation of each analyzed slice from the mean energy, using the theoretical energy- and angle-dependence calculated with the Nijmegen PWA93 solution [5].

The *np* scattering angle was determined event by event with a resolution dominated by the multiple Coulomb scattering of the outgoing proton in the $CH_2$ target material. The rms multiple scattering angle through half the target thickness (assuming an average scattering vertex at the center plane of the target) varied from 1.0° for forward protons to 2.3° for the largest-angle protons analyzed. In contrast, the angle of the incident neutron was determined from the tagging with a typical resolution $\sigma \approx 2$ mrad [17]. To keep corrections for resolution smearing of the angular distribution small (see Sec. V D), the data were analyzed in 3° wide lab angle bins.

The cross sections for the three data subsamples, with their independently determined absolute scales, are mutually consistent in both magnitude and angular shape, within statistical uncertainties, as revealed by the comparisons in Fig. 13. The figure shows the relative difference, $((\frac{d\sigma}{d\Omega})_{\rm sampleA} - (\frac{d\sigma}{d\Omega})_{\rm sampleB})/(\frac{d\sigma}{d\Omega})_{\rm sampleB})$, between pairs of cross sections for the three data samples. The reduced $\chi^2$ value for the comparison of each pair of samples is indicated in the legend to Fig. 13. This comparison supports the reliability of the experiment and analysis, because these samples come from complementary regions of the tagged beam spatial and energy profiles (see Fig. 4) and are subject to somewhat different systematic error concerns. We view the agreement in absolute cross section scale as a particularly significant demonstration of the accuracy of the neutron profiles reconstructed from tagging and of the subtraction procedure applied to remove corrupted events from the 2-stop sample (see Sec. III B). Cross sections extracted for different time periods within the production runs, and with different sets of cuts, are also consistent within uncertainties.

The results, averaged over all three data samples, are compared in Fig. 14 with previous experimental results at 162 MeV [7] and with the Nijmegen partial wave analysis (PWA93) at the two relevant energies [24]. The measured points are plotted at the yield-weighted centroid angle of each analyzed bin. The comparison of the present results with previous experiments and with partial wave analyses is discussed in detail in Sec. VI, after first describing the

TABLE I. Correction factors and systematic uncertainties in correction factors for the *np* cross sections.

| Source | Correction factor ($c_i$) | Uncertainty in $c_i$ |
|---|---|---|
| Accid. tagger coinc. | 1.0003 | $<\pm 0.001$ |
| Non-$^2$H tagger background | 1.0067 (2-stop); 1.0044 (1-punch) | $\pm 0.002$ |
| *n* pos'n unc. on $CH_2$ | 1.0000 | $\pm 0.001$ |
| *n* atten'n before $CH_2$ | 1.005 | $\pm 0.0025$ |
| Sequential react'ns & $x_{\rm tag}(n)$ errors | 1.063 | $\pm 0.010$ |
| C bkgd. subtraction | 1.0000 | $\pm 0.004$ |
| H in C target | 1.000 | $\pm 0.004$ |
| Corrupted event subtraction | 1.000 | $< \pm 0.001$ |
| Software cut losses | 1.010 | $\pm 0.005$ |
| Reaction tail losses | 1.004 | $\pm 0.002$ |
| Neutron polarization effects | Angle-dependent: $<1.0012$ (1-punch) $>0.9986$ (2-stop) | $\pm 0.001$ |
| $CH_2$ tgt. thickness | 1.0000 | $\pm 0.004$ |
| *np* scattering acceptance | 1.0000 | $\leqslant \pm 0.001$ ($>120°$) $\rightarrow \pm 0.017$ (90°) |
| MWPC inefficiency | 1.017 | $\pm 0.002$ |
| Trigger inefficiency | $1.002 + 0.008 \times \cos^2(\theta_p^{\rm lab})$ | $\pm[0.001 + 0.004 \times \cos^2(\theta_p^{\rm lab})]$ |
| Dead time diffs. | 0.991 | $\pm 0.005$ |
| Scattering angle errors | 1.000 | Angle-dependent, $\leqslant \pm 0.004$ |
| Angle resolution (mult. scattering) | Angle-dependent: 0.946 – 1.014 | $\pm 0.001$–$0.005$ |
| **Net, typical** | $\approx 1.10$ | $\approx \pm 0.016$ |

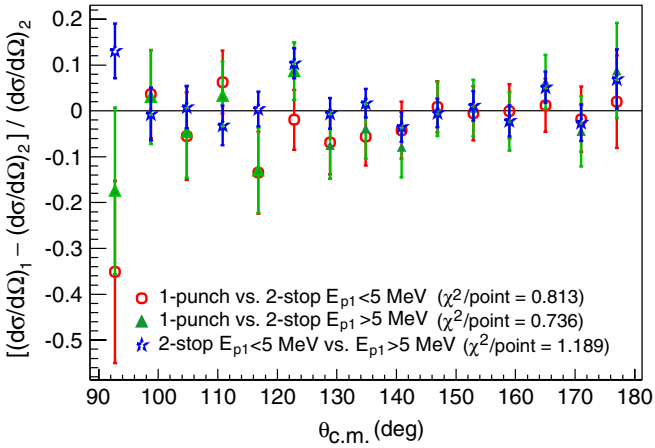


FIG. 13. (Color) The fractional differences between the absolute differential cross sections extracted for different analyzed data subsamples. The plotted error bars take into account only the independent statistical (including those from background subtractions) uncertainties for the three samples. Slightly different correction factors $c_i$ were applied to the cross sections for different samples, as indicated in Table I, before the comparison was made.

nature and evaluation procedure for each of the systematic uncertainties included in Table I.

## V. SYSTEMATIC ERRORS

Most of the individual correction factors $c_i$ applied to the extracted cross sections, and their associated systematic uncertainties listed in Table I, have been evaluated via complementary analyses of the data. In this section we briefly describe the procedures used and error estimates for each, being careful to distinguish uncertainties that affect only the overall cross section normalization from those with appreciable angle dependence. In the latter cases, we also characterize the degree of correlation among the uncertainties at different angles to facilitate inclusion of the uncorrelated systematic errors in PWAs including the present data. For purposes of logical flow, we organize the discussion into four categories: (A) tagged neutron flux uncertainties; (B) *np* backscattering yield uncertainties; (C) target thickness, acceptance, and efficiency uncertainties; and (D) errors in determining the kinematic variables. In Sec. V E we present a summary of the angle-dependent systematic errors.

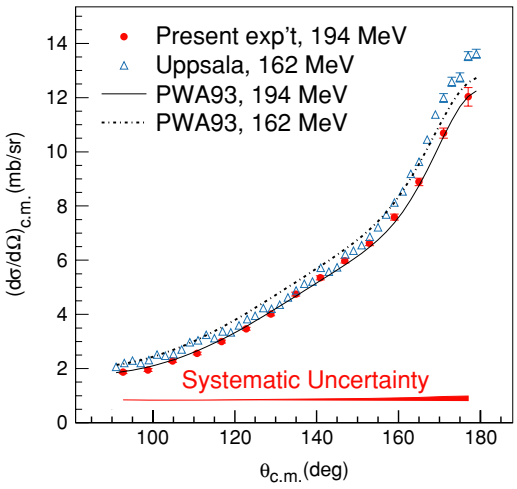


FIG. 14. (Color online) Absolute differential cross section from the present experiment compared with data from Ref. [7] and with PWA calculations at two relevant energies. The error bars on the present results are statistical, including background subtraction. The width of the shaded band at the bottom, representing the net absolute systematic uncertainty, including that in the overall normalization, is comparable to or smaller than the statistical error at each angle.

### A. Tagged neutron flux uncertainties

The sources below contribute to uncertainties in extracting the angle-integrated yields $N_{1,2,3}$ in Eq. (1), dominated by the noninteracting tagged neutrons in event stream 1. All of the issues discussed in this subsection give rise to overall (angle-independent) normalization errors in the differential cross sections.

#### *1. Accidental tagger coincidences*

Accidental coincidences between two uncorrelated particles detected in the tagger contribute slightly to the apparent tagged neutron flux on the secondary target, leading to an underestimate of the cross section. The accepted events in all three event streams passed a cut on the time difference $\Delta t = (t_{p1} - t_{p2})$ between the two tagger hits, as indicated in Fig. 15. The correction factor was determined from the ratio of events in stream 1 that passed all other cuts defining the tagged neutron beam but fell within one of two displaced time windows, $|\Delta t + 110\,\text{ns}| \leqslant 70$ ns and $|\Delta t - 170\,\text{ns}| \leqslant 70$ ns, to the yield in the prompt coincidence window $|\Delta t - 30\,\text{ns}| \leqslant 70$ ns. The resulting correction factor is $c_1 = 1.0003$, with an uncertainty $< \pm 0.001$, showing that accidental coincidences were a minor issue for the experiment.

#### *2. Tagger background from non-$^2$H sources*

Additional possible background contributions to the tagged neutron flux could arise from real (correlated) two-particle coincidences in the tagger, generated by proton beam interactions with nuclei heavier than deuterium in material displaced from the GJT. This possibility was checked via runs where hydrogen gas was substituted for the deuterium in the GJT to induce similar beam "heating" without any real possibility of tagged neutron production (since the proton beam energy was far below pion production threshold for the *pp* system). A correction factor $c_2 = 1.0044 \pm 0.002\,(1.0067 \pm 0.002)$ for 1-punch (2-stop) events was determined from the ratio of accidental-subtracted tags satisfying the tagged neutron conditions with the hydrogen vs deuterium production targets. The statistical uncertainties in these ratios were considerably smaller than $\pm 0.002$; the quoted uncertainty is intended to allow for the possibility of slight systematic differences in beam heating, hence in the rate of interactions with displaced material, between the two GJT gases.

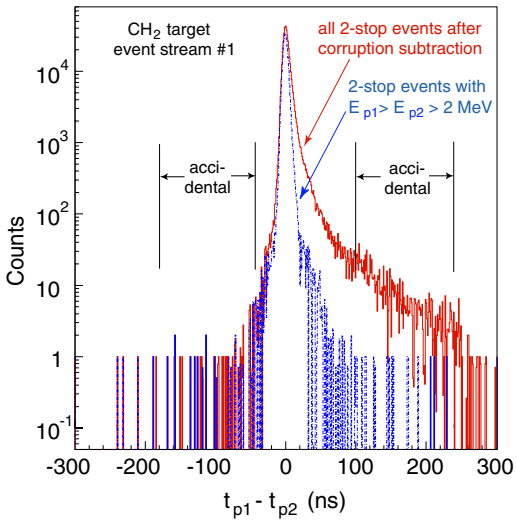


FIG. 15. (Color online) The distribution of DSSD arrival time difference between the two recoil protons for tagged neutron events, shown for all 2-stop events (following subtraction of the corrupted events as per Sec. III B) and for 2-stop events where the lower of the two DSSD energy depositions ($E_{p2}$) exceeds 2.0 MeV. The vertical lines indicate the prompt coincidence gate (central region between the inner two lines) imposed in the analysis, plus two displaced gates used to assess accidental coincidence background in event stream 1. The long tail seen for events with $E_{p2} \leqslant 2.0$ MeV, arising from detector noise and imperfect software corrections for time walk near the front-end discriminator threshold, leads to an overestimate of the accidental coincidence yield, but the correction and uncertainty still remain quite small.

#### 3. *Impact position uncertainty on the* $CH_2$ *target*

This is the first of several error sources we consider that arise when a properly tagged neutron does not reach the $CH_2$ (or C) secondary target, or reaches it at a significantly different position than expected from the tagging. Because of the finite (several mm) impact position resolution from the tagger, some tagged neutrons predicted to hit the secondary target may actually miss it, while some predicted to miss the target may hit it. Especially near the target edges, where the yield of *np* scattering events drops rapidly and nonlinearly as a function of impact position, this resolution smearing can affect the extracted cross sections. In practice, however, we observe no statistically significant difference in cross section normalization between the independent event samples from the bulk of the target ($|x_{\rm tag}| \leqslant 9.0$ cm and $|y_{\rm tag}| \leqslant 9.0$ cm) and from a 5.0-mm-wide strip ($9.0 < |x_{\rm tag}| \leqslant 9.5$ cm or $9.0 < |y_{\rm tag}| \leqslant 9.5$ cm) surrounding this core. From this comparison and the fraction of all events arising near the target edges, we infer a correction factor $c_3 = 1.000 \pm 0.001$.

#### 4. *Neutron attenuation before the* $CH_2$ *target*

Some tagged neutrons fail to hit the secondary target, leading to an underestimate of the extracted *np* cross section, as a result of interactions they undergo upstream of that target. Approximately 3.5% of 200 MeV neutrons will undergo an inelastic reaction of some sort in the upstream material [25], which is dominated by the 0.29-cm-thick stainless steel vacuum window at the exit of the Cooler's 6° magnet vacuum chamber, the 0.64-cm-thick LUV plastic scintillator, and the 0.64-cm-thick SUV plastic scintillator (the first two of these traversed at an incidence angle ≈14°). However, many of these "prescattering" neutrons give rise to charged products that get vetoed by LUV or SUV (and hence do not contribute to the tagged flux) or are removed by the C subtraction as apparent *np* scattering events from an upstream source. Others yield an energetic neutron or proton, not strongly deflected from the original tagged neutron trajectory, that still strikes the nearby secondary target with a chance to induce a tertiary interaction there, and so might still be considered as part of the incident flux.

We may judge the rate of such tertiary interactions from events where a forward proton emerges from the secondary target at a transverse location ($x_{\rm track}$, $y_{\rm track}$) substantially different (by much more than the tagging position resolution effect considered in Sec. V A3) from the predicted impact position of the tagged neutron ($x_{\rm tag}$, $y_{\rm tag}$). Such tertiary interactions introduce their own problems in the analysis, to be addressed separately in the next subsection. Here, we study them to place limits on the probability of larger-angle upstream scattering, which yields no chance of a tertiary scattering. In Fig. 16, we show the difference spectra for $x_{\rm track} - x_{\rm tag}$ and $y_{\rm track} - y_{\rm tag}$ for 1-punch events (to eliminate ambiguities from the corrupted 2-stop events seen in Fig. 6) after $CH_2$-C subtraction (to eliminate ambiguities from *np* scattering induced on material displaced from the secondary target). The narrow Gaussian resolution peaks sit atop a broad background that has important contributions from these tertiary interactions.

By fitting the background in Fig. 16 with a broad Gaussian, and assuming that the probability of initiating a scattering in the secondary target is roughly the same for the prescattered neutrons as for the bulk of the tagged neutrons, we estimate that 0.5% of tagged neutrons may be prescattered through a sufficiently large angle to cause a transverse displacement greater than 10 cm (i.e., half the target width or height) on the secondary target. We use this estimate to infer a correction factor $c_4 = 1.005 \pm 0.0025$ for tagged neutron prescattering flux losses before the $CH_2$ target. The ±50% uncertainty we assign to $(c_4 - 1)$ is intended to account for non-prescattering

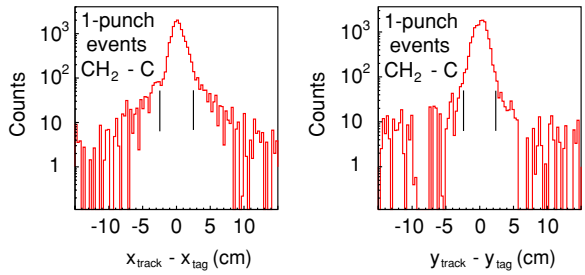


FIG. 16. (Color online) The difference distributions in $x$ (left) and $y$ (right) coordinates determined from tracking of the forward proton vs reconstruction of the tagged neutron, for the 1-punch data sample after $CH_2$-C subtraction. The vertical lines indicate the location of software gates used to remove events that may be complicated by sequential reactions or tagging errors.

origins of the background in Fig. 16 (e.g., tagging errors or sequential reactions *within* the $CH_2$ or tertiary scattering of a forward proton in material *following* the $CH_2$ target) and for possible upstream neutron interactions that elude the above analysis.

#### *5. Sequential reactions in the secondary target or upstream material*

Here we deal explicitly with the events contributing to the broad backgrounds in Fig. 16 and in the analogous distributions for 2-stop events. From the behavior of these events and the differential cross sections we extract specifically from them, we judge them to correspond primarily to valid free *np* scattering in $CH_2$ either following an earlier interaction of the tagged neutron or preceding a later interaction of the forward proton. The two interactions will in some cases both have taken place within the $CH_2$ target. Some of the background may also arise from tagging errors associated with less than complete energy collection for the recoil protons in the tagger. A more quantitative decomposition of the observed background among these sources is discussed below. Regardless of their detailed source, the events in the tail regions of Fig. 16 are distorted because we mismeasure the scattering angle and possibly the incident neutron energy for the free *np* scattering. While a small fraction of the events within the *peak* regions in Fig. 16 may also be affected by (forward) sequential reactions, we consider them to be a valid part of the analyzed sample because the agreement between tracking and tagging demonstrates that the *np* scattering angle has been measured within our experimental resolution for all these events.

The least biased way to handle the tail events in Fig. 16 is to eliminate them from the analyzed sample. This is simple enough to do for each angle bin in event stream 2, via the software cuts requiring $|x_{\rm track} - x_{\rm tag}| \leqslant 3\sigma_x$ and $|y_{\rm track} - y_{\rm tag}| \leqslant 3\sigma_y$, where $\sigma_x \approx 0.8$ cm and $\sigma_y \approx 0.7$ cm are the widths of the narrow Gaussian peaks in Fig. 16. (The widths are dominated by the longitudinal vertex uncertainty introduced by the secondary target thickness, see Sec. III C) These cuts combine to eliminate 6.3% of the event stream 2 ($CH_2$-C) yield, averaged over 1-punch and 2-stop samples and integrated over scattering angle. The fraction of events removed varies slowly with *np* scattering angle, increasing by an average factor of 1.2–1.3 as one goes from c.m. angles near 180° to those near 100°, thus slightly modifying the angular distribution shape of the extracted *np* differential cross section.

The fraction of events removed and its angle dependence are qualitatively consistent with expectations. Of the 3.5% of tagged neutrons that will undergo inelastic reactions upstream of the $CH_2$ target, we estimate that roughly 1.5% will escape being vetoed and hence will contribute to these tails. Another 2.6% of incident neutrons or outgoing protons are expected to undergo a second reaction in the $CH_2$, at normal incidence. However, proton postscattering grows in importance with the proton angle emerging from the primary *np* scattering, because the proton sees a thicker target at a lower energy (implying a larger reaction cross section). We thus expect roughly 5% of *np* scattering events to be removed from the peak to the tail regions in Fig. 16 via nuclear pre- and postscattering, with the fraction increasing slowly with increasing proton angle. This estimate is consistent with the 2.4% of events seen in the tails of the $y_{\rm track} - y_{\rm tag}$ distribution. The somewhat larger losses observed in the $x_{\rm track} - x_{\rm tag}$ tails suggest an additional contribution from tagger errors, which cannot depend on *np* scattering angle.

Removal of the tail events from the analyzed *np* scattering sample requires simultaneous removal of the neutron flux that leads to such compromised events. However, we have no access to analogous cuts for event streams 1 and 3, where there is no MWPC information. Hence, we introduce the (angle-independent) flux correction factor $c_5 = 1.063 \pm 0.010$ under the assumption that the events removed from event stream 2, integrated over angle, arise from the same fraction of the tagged neutron flux. (The actual correction factors applied differ for the three data samples, reflecting differences in the fraction of events removed by these cuts.) The uncertainty allows for errors in this assumption, for example, because it neglects the energy dependence of the *np* scattering probability in the $CH_2$ target. The uncertainty is also intended to encompass the possible exclusion of valid single-scattering *np* events in the extreme (beyond $\pm 3\sigma$) tails of the resolution profile and the possible inclusion of events (lying beneath the peaks in Fig. 16) slightly affected by sequential reactions. This is the largest single correction and systematic uncertainty we apply.

### B. Uncertainties in absolute *np* backscattering yields

Analysis issues in the extraction of the free scattering yield $N_2(\theta)$ needed in Eq. (1) can lead, in principle, to angle-dependent errors. We thus specify for each case below whether the estimated uncertainty should be considered as angle dependent and as uncorrelated from angle bin to bin.

#### *1. Uncertainties in background subtraction via the* C *target*

As described in Sec. III C, we relied heavily on the $CH_2$-C subtraction to remove simultaneously backgrounds due to quasifree scattering from carbon nuclei in the secondary target and to reactions induced on displaced sources. The precision of the subtraction depends on that of our knowledge of the relative target thicknesses and integrated neutron flux exposures for the $CH_2$ vs C runs and on the stability of beam conditions between the two sets of runs. The relative normalization, taken from cleanly (kinematically) identified *pd* scattering yields measured simultaneously, is determined with quite high statistical precision but could, in principle, deviate systematically from the more relevant ratio of tagged neutron yields. The overall precision of the relative normalization was judged from the extent to which scattering events from the aluminum target platform [see Fig. 8(a)] were successfully removed by the C subtraction. We concentrate first on this background source because its yield is not sensitive to the $CH_2$/C target thickness ratio.

The reconstructed $y_{\rm tag}$ distributions in the vicinity of the aluminum platform peak, for both $CH_2$ and C targets (see Fig. 8), could be well reproduced by the sum of a Fermi distribution and a polynomial to represent the bottom target

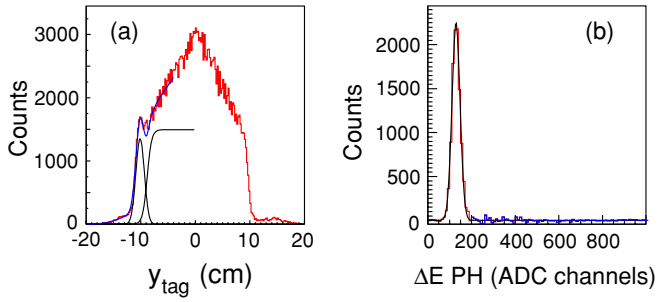


FIG. 17. (Color online) The reconstructed (a) $y_{tag}$ spectrum for the $CH_2$ target before background subtraction and (b) $\Delta E$ pulse height spectrum for $CH_2$-C for the $\theta_p^{sc}$ bin 3°–6°. The superimposed curves in both frames represent fits used in estimating background subtraction accuracy.

edge and a Gaussian to represent the aluminum peak. The fit for the $CH_2$ is shown in Fig. 17(a). An analogous fit was then carried out for the C-subtracted spectrum in Fig. 8(b), fixing the positions and widths of the Gaussian and Fermi-function contributions to their common values for $CH_2$ and C. The ratio of events in the Gaussian peak after subtraction to that before subtraction is $(1.9 \pm 0.54) \times 10^{-3}$, providing one measure of the accuracy of the background subtraction.

An independent measure was provided for each *np* scattering angle bin by the fraction of high energy-loss tail events that survive the subtraction in $\Delta E$ pulse height spectra [see Fig. 8(c)]. The tail events were integrated by summing all counts at $\Delta E$ values more than $4\sigma$ above the center of a Gaussian fitted to the free scattering peak, as illustrated in Fig. 17(b). For the three largest $\theta_p^{sc}$ bins studied, this approach breaks down because the free scattering $\Delta E$ peak develops a substantial Landau tail and is no longer well reproduced by a Gaussian shape. But for all (12) smaller-angle bins, the ratio of tail events after to before C subtraction fluctuates about zero, with a weighted average over angle bins of $(2.97 \pm 0.24) \times 10^{-3}$. This measure is sensitive to the target thickness ratio as well as to the relative flux normalization for $CH_2$/C. The two measures combined do not give compelling evidence of a need for any correction and are conservatively summarized by associating with the C subtraction an angle-independent correction factor $c_6 = 1.000 \pm 0.004$.

The uncertainty estimated in this way also subsumes two other potential sources of systematic error. One is accidental coincidences between a real tagged neutron and an uncorrelated forward-going proton emerging from the GJT or the Cooler beam pipe (the most abundant sources of protons). To the extent that such coincidences passed all our cuts, they might have contributed to $N_2(\theta)$ for the $CH_2$ target. However, since these accidentals are independent of the presence or nature of the secondary target, they would be subtracted via the C target measurements. The second effect concerns possible proton attenuation before the hodoscope, which is required as part of the event stream 2 hardware trigger. The dominant material between secondary target and hodoscope that might have served as a source of such proton losses is the $\Delta E$ scintillator, where tertiary interactions should cause abnormal energy loss. Since the $c_6$ uncertainty estimate includes allowance for such abnormal pulse heights in carbon-subtracted $\Delta E$ spectra, it should also include such proton attenuation effects.

One further potential complication with the background subtraction could have arisen if there had been any appreciable hydrogen buildup on the graphite target used for the subtraction, a possibility limited by the hydrophobic nature of graphite. In this circumstance we would subtract some small fraction of the valid free scattering events and thus would introduce an effective overall normalization error in the hydrogen target thickness $t_H$ used in Eq. (1). To estimate this effect we considered *np* scattering events forward of $\theta_{c.m.} = 90°$, where event stream 2 contained some coincidence events, with a forward-scattered neutron detected in the hodoscope and the larger-angle proton detected in the $\Delta E$ scintillator and (at least) the front two MWPCs. The angle of the proton was determined from MWPC ray-tracing, whereas that of the neutron was deduced from the hodoscope elements fired and from the position inferred from the time difference between hodoscope phototubes mounted at the two ends of each element [17]. The opening angle spectrum reconstructed for such *np* coincidence events exhibited a clear free scattering kinematic peak for the $CH_2$ target, but only the Fermi-smeared and acceptance-limited angular correlation characteristic of quasifree scattering for the C target (see Fig. 18). Figure 18 includes fits to the distributions for both targets based on the sum of a quadratic background and a Gaussian free scattering peak, with the peak location and width fixed for the C target to the values determined from $CH_2$. The fit for C is statistically consistent with no hydrogen content in the graphite target, with a $1\sigma$ limit on the hydrogen thickness of 0.4% that of the hydrogen in $CH_2$. We thus apply a cross section correction factor $c_7 = 1.000 \pm 0.004$ for hydrogen in the C target.

#### 2. *Uncertainty in subtraction of corrupted events*

For the 2-stop event stream, we followed the procedure described in Sec. III B to subtract the punch-through events that had been corrupted by the electronic loss of backing detector pulse height information. There is no evidence for any systematic deviation in distribution shapes between the corrupted sample and our simulation of this sample using valid recorded punch-through events. Thus, the only uncertainty we consider is that in the normalization of the simulated sample to the corrupted events in stream 2. The normalization factors were determined from fits for the subsample of corrupted events that had valid backing detector timing signals, and the uncertainty in these normalization factors was then deduced from the change in normalization factor that caused an increase of unity in the overall $\chi^2$ value for the fit. The effect of this normalization uncertainty on the extracted 2-stop cross sections was typically ≈0.01% and is negligible in comparison with other systematic errors. Hence, we assign a correction factor $c_8 = 1.000$ with uncertainty $< \pm 0.001$ to the subtraction of corrupted events.

#### 3. *Losses via software cuts*

The efficiency of software cuts applied to event stream 2, but not to streams 1 and 3, was judged by comparing

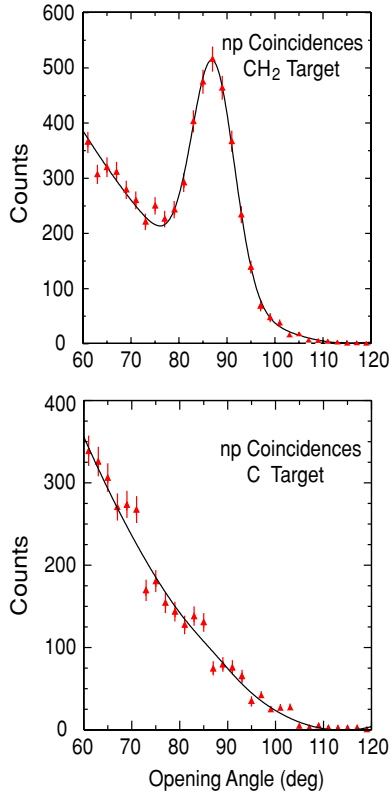


FIG. 18. (Color online) *np* scattering opening angle spectra reconstructed for events where a large-angle proton fires at least the first two MWPCs and a forward neutron appears to fire the rear scintillator hodoscope. For such coincidence events, a clear free scattering peak is seen with the $CH_2$ production target (upper frame), whereas no hint of such a peak is seen for the C target (lower). The solid curves are fits with a Gaussian peak superimposed on a quadratic background. The distribution shape for C reflects the quasifree *np* scattering opening-angle spectrum convoluted with the coincidence acceptance of the forward detector array.

the ratio of cross sections obtained, after $CH_2$-C subtraction, for all events failing vs satisfying a given cut. The most important of these cuts were on $\Delta E(\theta_p^{\rm sc})$ (see Fig. 9) and on $x_{\rm track} - x_{\rm tag}$ and $y_{\rm track} - y_{\rm tag}$. The latter cuts were already dealt with in Sec. V A5. (Another cut, on the quality of track fits, is treated together with wire chamber inefficiencies below.) The $\Delta E$ cut limits were somewhat tighter than the $4\sigma$ allowance used in estimating background subtraction accuracy (see Sec. V B1). We found the ratio of background-subtracted events failing/satisfying the $\Delta E$ cut to be 1.0%, averaged over all event streams and angles. There is no evidence for any significant angle dependence in this loss, but there are strong enough fluctuations in the losses from angle to angle or event stream to event stream that we assign a ±50% uncertainty to the losses. We thus apply a corresponding, angle-independent correction factor $c_9 = 1.010 \pm 0.005$. With this systematic uncertainty, application of the $\Delta E$ cut still reduced the overall cross section error bars slightly because the quasifree background to be subtracted decreased significantly.

#### 4. Reaction tail losses beneath the hodoscope energy threshold

Because we did not use any software cuts on energy deposition in the rear hodoscope, we avoided the large corrections that would have been needed to account for protons lost to nuclear reactions in this hodoscope (see Fig. 10). However, if the reaction is sufficiently severe that the deposited energy falls below the hodoscope hardware threshold, then the event will have been lost in hardware to a trigger inefficiency. To estimate these potential losses, we fit the hodoscope energy spectra after $CH_2$-C subtraction to the sum of a Gaussian and an exponential (reaction) tail, as shown in Fig. 10. The tail was extrapolated to zero energy deposition, and the ratio of yields below to above threshold (typically set at 5–10 MeV proton energy) was thereby estimated. The loss below threshold was found to be quite consistent with 0.4% for each scattering angle bin, so that we again have applied an angle-independent correction factor $c_{10} = 1.004 \pm 0.002$.

#### 5. Neutron polarization effects

While the stored proton beam in the Cooler was unpolarized for this experiment, the neutron production reaction selected neutrons scattered to one side of the beam (beam right) at about 14° in the laboratory frame. At this angle, the $^2$H$(p, n)$ charge exchange reaction that dominates our tagged beam production has a small polarization, so the beam neutrons would have been slightly polarized vertically (perpendicular to the horizontal production plane). The magnitude of this effect is $P_n^{\rm prod} \approx -0.1$, where the minus sign indicates that, for neutron production to the right of the cooled proton beam, the neutron spin points preferentially downward at the secondary target. The tagged neutron polarization can then give rise to a left-right asymmetry in *np* scattering events:

$$\varepsilon_{np}(\theta, \phi) \equiv P_n^{\rm prod} A_{np}(\theta) \cos(\phi). \tag{2}$$

Measurements and phase shift solutions at intermediate energies [24] show the *np* scattering analyzing power, $A_{np}$, to be a strong function of scattering angle, but with magnitude no larger than 0.12 over the angle range of interest for the present experiment. The $\cos(\phi)$ factor reflects the fact that it is only the component of the vertical neutron polarization perpendicular to the scattering plane for a given *np* event that matters.

Because the scattering yield is simply redistributed between scattering toward the left and the right, there would be no effect at all on cross sections measured with a fully left-right symmetric forward detector array. Thus, the only residual polarization effect changes the measured yield by a fraction:

$$\delta(\theta) = P_n^{\rm prod} A_{np}(\theta) \int_0^{2\pi} a(\theta, \phi) \cos(\phi) d\phi \Big/ \int_0^{2\pi} a(\theta, \phi) d\phi, \tag{3}$$

where $a(\theta, \phi)$ is the fractional detector acceptance (determined from fits such as those in Fig. 11) in the specified angle bin. The sign convention used here is that positive $\delta(\theta)$ implies that we observe a higher event stream 2 yield than we should in the corresponding $\theta_p^{\rm sc}$ bin, necessitating a correction factor $c_{11}(\theta_p^{\rm sc}) = 1.0 - \delta(\theta)$.

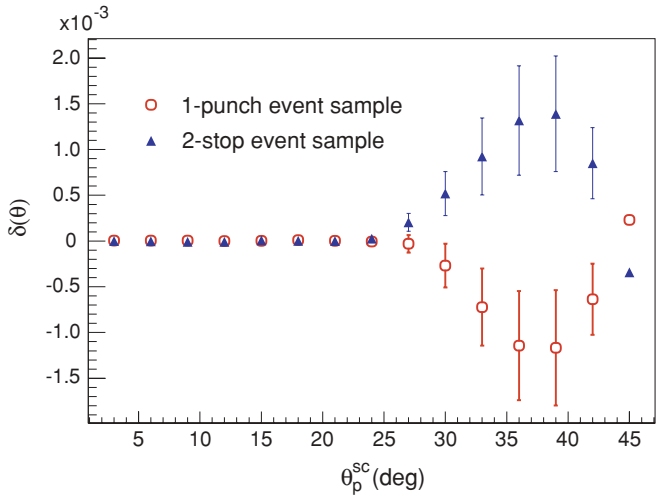


FIG. 19. (Color online) The estimated fractional cross section error introduced by neutron polarization effects for the 1-punch and 2-stop event samples, plotted as a function of *np* scattering angle.

Figure 19 shows the $\delta(\theta)$ distribution calculated for 1-punch and 2-stop data samples from Eq. (3), taking $A_{np}(\theta)$ from Nijmegen PWA93 calculations [24]. We find $\delta = 0$ for both samples at all angles $\theta_p^{\rm sc} \lesssim 25^\circ$, because the detector has full azimuthal acceptance in that region. The small corrections have opposite sign, and hence tend to cancel, for the two samples at larger angles because the 2-stop events preferentially populate the left side of the secondary target, while the 1-punch events originate mostly on the right (see Fig. 4). The latter difference is reflected in their respective $a(\theta, \phi)$ functions (see Fig. 11) used in Eq. (3).

While the *np* analyzing power and the forward detector acceptance functions are well determined in this experiment, we assign a significant uncertainty to the average tagged neutron polarization, $P_n^{\rm prod} = -0.10 \pm 0.05$, to account for contributions from production mechanisms other than charge exchange. There is correspondingly a $\pm 50\%$ uncertainty assigned to each value of $\delta(\theta)$ in Fig. 19, but these errors are completely correlated from one angle bin to another and are strongly correlated between 2-stop and 1-punch data samples. The largest net uncertainty from neutron polarization after the (separately corrected) 1-punch and 2-stop results are combined is $\pm 0.6 \times 10^{-3}$, and so we conservatively assign an angle-independent uncertainty of $\pm 0.001$ to $c_{11}$.

### C. Target thickness, acceptance, and efficiency errors

#### 1. $CH_2$ *target thickness uncertainty*

The overall normalization uncertainty associated with $t_H$ in Eq. (1) was determined to be $\pm 0.4\%$ (i.e., $c_{12} = 1.000 \pm 0.004$) from careful weighing of the $CH_2$ target used. The carbon-to-hydrogen ratio in the target was precisely constrained by the target material. The target consisted of Tivar 1000, an ultra-high-molecular-weight ($6.2 \times 10^6$ u) polyethylene. Two extra hydrogen atoms per molecular chain (one on each end) cause a negligible ($2 \times 10^{-6}$) deviation from the nominal 2.000 hydrogen/carbon atom ratio. Because the target only sat in a secondary neutron beam of low flux, there should not have been any appreciable deterioration in the target during the length of the run, nor was any visually evident.

#### 2. *Acceptance uncertainty*

The acceptance uncertainty was determined independently for each angle bin by varying the most critical one or two detector geometry parameters used in the simulations (see Fig. 11) from their best-fit values until the overall $\chi^2$ value for the simulated vs measured $\phi_p^{\rm sc}$ distribution in that angle bin increased by unity. Because the optimized values of $\chi^2$ per degree of freedom for the different angle bins and event samples were statistically distributed about 1.14, rather than 1.00, we multiplied these acceptance changes by a uniform factor of 1.07 to arrive at final systematic uncertainties. The acceptance uncertainty is strongly angle dependent, varying from $\pm 0.001$ at $\theta_{\rm c.m.} > 120^\circ$, where $a_\phi > 95\%$, to $\pm 0.017$ at $\theta_{\rm c.m.} = 90^\circ$, where $a_\phi \approx 50\%$. With this evaluation method, we consider the estimated uncertainties to be largely uncorrelated from angle bin to bin.

#### 3. *Wire chamber efficiencies*

The MWPCs were not used at all in forming a hardware trigger, but in software event reconstruction we required at least one hit registered in each of the $x$ and $y$ planes, for chambers 1, 2, and 3, plus a $\chi^2$ value below an upper threshold for fitting these hits to a straight line track. Thus, the overall MWPC efficiency to use in extracting absolute cross sections is

$$\eta_{\rm MWPC} = \eta_x(1)\eta_y(1)\eta_x(2)\eta_y(2)\eta_x(3)\eta_y(3)\eta_{\rm fit\ quality}. \quad (4)$$

The efficiency of each MWPC plane was determined from tracks reconstructed without the benefit of the plane in question, based on the fraction of such tracks that produced a hit on this plane in the immediate vicinity of the reconstructed crossing point. Each of the first six factors in Eq. (4) was found to exceed 0.99 and was determined with an uncertainty $\approx \pm 5 \times 10^{-4}$. Their product is $0.985 \pm 0.0013$.

The factor $\eta_{\rm fit\ quality} = 0.998 \pm 0.0011$ was determined by estimating the number of free scattering events removed from the analysis by the $\chi^2$ cut. This was done by examining $\Delta E$ spectra for individual angle bins, following carbon subtraction, for events that failed the fit quality test. The number of free scattering events (and its uncertainty) in each such spectrum was extracted by fitting Gaussian peaks of the same position and width as those used for the normal $\Delta E$ spectra, such as Fig. 17(b). There was no indication in these analyses that any of the factors in Eq. (4) varied with position on the MWPCs, or therefore with scattering angle. The overall wire chamber efficiency correction is thus an angle-independent $c_{14} = 1.0017 \pm 0.002$.

#### *4. Trigger inefficiencies*

Inefficiencies in detectors used to form the hardware trigger lead to loss of events in an unrecoverable way. Possible tagger inefficiencies do not matter here, because they lead to loss of the same fraction of events from streams 1, 2 and 3 and, hence, do not affect the cross sections determined from ratios of event yields in these streams. The two detectors used to form the hardware trigger for event stream 2, but not for stream 1, are the $\Delta E$ scintillator and the rear hodoscope. The former was viewed by four phototubes, at least three of which were required to give signals surpassing threshold in the trigger logic. In the data analysis, we were able to determine for each scattering angle bin the ratio of reconstructed free scattering events that had only three vs all four $\Delta E$ phototubes above threshold. We then estimated the $\Delta E$ trigger inefficiency under the conservative assumption that the ratio of free scattering events with two or fewer phototubes firing to those with three firing would be the same as the determined ratio of events with three to four firing. (Some illuminated locations on the scintillator lacked a direct line of sight to one or another, but never simultaneously to two, of the four phototubes.) The resulting inefficiency appears to show a systematic angle dependence, roughly represented by $0.008\cos^2(\theta_p^{\rm sc})$; i.e., the inefficiency grows as the $\Delta E$ pulse height shrinks.

We have considered two different types of potential hodoscope trigger inefficiencies. Problems in an individual hodoscope element or phototube would show up as an inefficiency localized in $\theta$ and $\phi$ and, therefore, as a deviation of the measured $\phi$ distribution for some angle bins from the simulated acceptance function. Any such localized trigger-level inefficiencies should thus be subsumed in the acceptance uncertainty calculation mentioned above.

However, an electronic inefficiency in the modules forming the hodoscope trigger logic could have caused equal fractional losses in all angle bins. A limit on this inefficiency was estimated from event stream 4 (observing tagged protons from the GJT), which included the Veto2 scintillator directly in front of the hodoscope, but not the hodoscope itself, in the trigger logic. We found that $(0.6 \pm 0.1)\%$ of these triggered events were not accompanied by hodoscope signals above threshold in both relevant phototubes, of which 0.4% have already been accounted for as reaction tail losses below threshold (see Sec. V B4).

Combining the above effects, the overall correction factor for trigger inefficiencies has been taken as $c_{15} = [1.002 + 0.008 \times \cos^2(\theta_p^{\rm sc})] \pm [0.001 + 0.004 \times \cos^2(\theta_p^{\rm sc})]$. The angle-dependent part of the uncertainty here is intended to accommodate observed fluctuations in the inferred $\Delta E$ trigger efficiency and is viewed as largely uncorrelated among different angle bins.

#### *5. Dead time differences among event streams*

Triggers in all event streams were blocked electronically at an early stage in the event trigger logic by a common busy signal reflecting electronic readout or computer processing activity in *any* of the event streams. To first order, then, the different streams should have a common dead time ($\approx$10% for typical running conditions), and the dead time should cancel in the event stream ratios from which cross sections are deduced [see Eq. (1)]. However, this cancellation is imperfect, as revealed by ratios of scaler values recording the number of tagged neutron vs tagged proton candidates before and after busy-vetoing. Typically, $\approx$1% fewer neutron tags survived the veto, and this was traced to the occurrence of bursts of electronic noise triggers from the tagger. While the loss of these noise triggers should not have directly depleted the valid sample of any event streams (i.e., (2)–(4)) that required other detectors in coincidence with the tagger, it did reduce the number of valid events recorded in the neutron flux stream (1), because all raw neutron tags, whether valid or not, contributed equally to the countdown of a (divide by 20) prescaler used for this stream. To compensate for this loss of neutron flux events, we must reduce the extracted cross sections at all angles by a factor $c_{16} = 0.991 \pm 0.005$. The uncertainty in this correction allows for possible model dependence in our interpretation of the live-time difference inferred from the scaler ratios.

### D. Errors in determination of kinematic variables for *np* scattering

#### *1. Neutron energy errors*

As explained in Sec. IV, the data were analyzed in narrow neutron energy slices, with each result then being corrected slightly to extract a final overall cross section at the single mean energy of 194.0 MeV. There is an overall scale uncertainty in the tagged neutron energies that we estimate to be $\pm$150 keV, with roughly equal contributions from the energy of the stored primary proton beam in the Cooler and the energies extracted from the tagger for the low-energy recoil protons. The stored beam energy (202.46 MeV) is based on the precisely measured rf frequency (1.96502 MHz) and the Cooler circumference, which has been previously calibrated [26] to better than 1 cm out of 87 m, translating to $\pm$70 keV. In the "coasting" (rf off) mode used for data taking, the beam energy is maintained by interactions with the cooling electrons, and this may increase the beam energy uncertainty to $\approx$100 keV. The energy scale of the recoil protons is calibrated by analysis of $^{228}$Th $\alpha$-source spectra measured with the tagger [17], and its $\pm$100 keV uncertainty arises predominantly from thickness uncertainties for detector dead layers, combined with the quite different corrections for energy loss in the dead layers needed for protons vs the calibration $\alpha$ particles.

The energy scale uncertainty could be translated into a consequent cross section uncertainty as a function of angle by using Nijmegen PWA93 calculations to evaluate

$$\delta\sigma_{\rm energy}\left(\theta_p^{\rm sc}\right) = (\pm 150\,{\rm keV})\frac{\partial[d\sigma/d\Omega]\left(\theta_p^{\rm sc}\right)}{\partial E}\bigg|_{194\,{\rm MeV}}. \quad (5)$$

Although this systematic error can be angle dependent, the values at different angles would still be completely correlated, since the neutron energy scale will be off in the same direction for all angles. Hence, we prefer to not include this effect in the cross section uncertainties, but rather to quote the measured

cross sections as applying at a mean neutron energy of 194.0 ± 0.15 MeV.

### 2. Scattering angle errors

A systematic error $\delta\theta_p^{\rm sc}$ in determination of the centroid $np$ scattering angle within a given analyzed bin is equivalent to an error $\delta\sigma_{\rm angle}(\theta_p^{\rm sc})$ in the measured differential cross section:

$$\delta\sigma_{\rm angle}\left(\theta_p^{\rm sc}\right) = \delta\theta_p^{\rm sc}\left.\frac{\partial[d\sigma/d\Omega]\left(\theta_p^{\rm sc}\right)}{\partial\theta_p^{\rm sc}}\right|_{194\,\rm MeV}, \qquad (6)$$

where the angular derivative of the cross section can be taken, for example, from Nijmegen PWA calculations [24]. In evaluating $\delta\theta_p^{\rm sc}$, we consider the contributions from uncertainties $\delta\theta_{\rm inc}$ in the neutron incidence angle on target deduced from the tagger and $\delta\theta_{\rm out}$ in the angle of the outgoing proton through the MWPCs:

$$\delta\theta_p^{\rm sc} = [\langle\delta\theta_{\rm inc}\rangle^2 + \langle\delta\theta_{\rm out}\rangle^2]^{1/2}, \qquad (7)$$

where the averages are evaluated over the full free scattering event sample, over the transverse coordinates $(x_{\rm tag}, y_{\rm tag})$ of the scattering origin on the secondary target, and over all scattering angles. Consistent values were extracted for the 2-stop and 1-punch samples.

The angle uncertainties were estimated within $1 \times 1$ cm$^2$ pixels in $(x_{\rm tag}, y_{\rm tag})$ as half the mean event-by-event difference between angles reconstructed by two different approaches. In the case of $\theta_{\rm inc}$ one method utilized tagger information only to predict the neutron trajectory, whereas the second considered instead the straight line from the neutron production vertex on the GJT, inferred from the tagger, to the intersection $(x_{\rm track}, y_{\rm track})$ of the reconstructed forward proton track with the secondary target. For $\theta_{\rm out}$ we used proton tracks reconstructed with MWPC geometry parameters that were either (i) optimized to minimize the overall $\chi^2$ value for tracks or (ii) adjusted to increase overall $\chi^2$ by unity. A yield-weighted average of the results over all target pixels gives $\langle\delta\theta_{\rm inc}\rangle = 1.3$ mrad and $\langle\delta\theta_{\rm out}\rangle = 0.04$ mrad.

The cross sections were not corrected for potential systematic angle errors, but we extract from Eq. (6) net systematic uncertainties of ±0.4% for $120 \leqslant \theta_{\rm c.m.} \leqslant 180^\circ$, ±0.3% for $100 \leqslant \theta_{\rm c.m.} \leqslant 120^\circ$, and ±0.1% for $90 \leqslant \theta_{\rm c.m.} \leqslant 100^\circ$. Because the extracted incidence angle differences (between the two methods described above) exhibit sizable fluctuations from one target pixel to another, or from one angle bin to another, we view these estimated uncertainties as uncorrelated from angle bin to angle bin.

### 3. Angle resolution smearing

Even if the centroid angle of each analyzed bin is determined accurately in the experiment, the angle resolution can lead to migration of events among bins and, hence, to a modification of the underlying angular distribution. For comparison with theoretical angular distributions, it is desirable to correct the experimental results for this smearing effect. The correction depends on the shape of the underlying angular distribution, the angle bin sizes, and the shape of the resolution profile associated with each bin. In the present case, we have excellent models for the shapes of both the underlying distribution (Nijmegen PWA93 [5,24]) and the resolution profile (a proton multiple Coulomb scattering Gaussian, neglecting single Coulomb scattering tails as these contribute to the sequential reaction tails already corrected in Sec. V A5). Furthermore, the angle bin sizes were chosen to be larger than the angle resolution width, keeping the smearing corrections small. We are thus able to make the corrections without relying on Monte Carlo simulations and their statistical limitations.

We consider protons redirected from their initial solid angle $d\Omega'$ at angles $(\theta', \phi')$ into the observed solid angle $d\Omega_{\rm meas}$ at $(\theta_{\rm meas}, \phi_{\rm meas})$ by multiple scattering through angle

$$\Delta\theta_{\rm ms} = \cos^{-1}[\cos\theta'\,\cos\theta_{\rm meas} + \sin\theta'\sin\theta_{\rm meas}\cos\phi']. \qquad (8)$$

The redirection contributes to the measured yield whether or not the initial direction $(\theta', \phi')$ falls within the detector acceptance. For given $\theta'$ and $\theta_{\rm meas}$, as $\phi' - \phi_{\rm meas}$ varies from 0 to $\pi$, $\Delta\theta_{\rm ms}$ varies from $|\theta' - \theta_{\rm meas}|$ to $\theta' + \theta_{\rm meas}$. The probability for multiple scattering into $d\Omega_{\rm meas}$ is taken to be a Gaussian, normalized to unit integral, of width dependent on $\theta'$ [27]:

$$P(\Delta\theta_{\rm ms})d\Omega_{\rm meas} = \frac{\exp\left[-\Delta\theta_{\rm ms}^2/2\delta\theta_{\rm rms}^2(\theta')\right]}{2\pi\,\delta\theta_{\rm rms}^2(\theta')}d\Omega_{\rm meas}, \qquad (9)$$

with rms angle [28]

$$\delta\theta_{\rm rms}(\theta') = \frac{13.6\,\text{MeV}}{T_p^{\rm lab}\left[1 + \left(1 + T_p^{\rm lab}/M_p\right)^{-1}\right]}\sqrt{\frac{0.233}{\cos\theta'}} \cdot\left[1 + 0.038\ln\left(\frac{0.233}{\cos\theta'}\right)\right], \qquad (10)$$

where $T_p^{\rm lab}$ is the lab energy in MeV of the outgoing proton, $M_p$ is the proton mass, and 0.233 is the number of radiation lengths corresponding to half the target thickness at normal incidence. The rms angles vary from 1.0° to 2.3° over the scattering angle range covered in the experiment.

The smeared (observed) differential cross section is then given by

$$\left(\frac{d\sigma}{d\Omega}\right)_{\rm lab}^{\rm smear}(\theta_{\rm meas}) = \frac{1}{\pi}\int_0^{\pi/2}\frac{\sin\theta' d\theta'}{\delta\theta_{\rm rms}^2(\theta')}\left(\frac{d\sigma}{d\Omega'}\right)_{\rm lab}^{\rm PWA93}(\theta') \cdot\int_0^{\pi} d\phi'\exp\left[-\Delta\theta_{\rm ms}^2/2\delta\theta_{\rm rms}^2(\theta')\right]. \qquad (11)$$

In writing Eq. (11), we have made the implicit assumption that the first and subsequent scatterings occur at spatial separations that can be neglected in comparison with the distance to the solid-angle-defining detectors. This is a good approximation for the present experiment, where the target is the dominant source of the multiple scattering. The resulting correction factors, by which the observed differential cross section must be multiplied to revert to the underlying distribution, are tabulated in

TABLE II. Final differential cross section results for *np* scattering at $E_n = 194.0 \pm 0.15$ MeV, averaged over data samples.

| c.m. angle (deg.) | Mult. scat. corr'n | $(d\sigma/d\Omega)_{\text{c.m.}}$ (mb/sr) | Stat. unc. (mb/sr) | Syst. unc.[a] (mb/sr) |
|---|---|---|---|---|
| 92.7 | 0.946±0.005 | 1.87 | 0.06 | 0.03 |
| 98.8 | 0.975±0.003 | 1.95 | 0.05 | 0.02 |
| 104.8 | 0.989±0.001 | 2.28 | 0.05 | 0.02 |
| 110.8 | 0.995±0.001 | 2.56 | 0.05 | 0.02 |
| 116.8 | 0.998±0.001 | 3.00 | 0.05 | 0.02 |
| 122.8 | 0.999±0.001 | 3.47 | 0.06 | 0.02 |
| 128.8 | 1.000±0.001 | 4.01 | 0.06 | 0.02 |
| 134.9 | 1.001±0.001 | 4.75 | 0.07 | 0.03 |
| 140.9 | 1.001±0.001 | 5.35 | 0.08 | 0.03 |
| 146.9 | 1.000±0.001 | 5.98 | 0.08 | 0.04 |
| 152.9 | 0.999±0.001 | 6.63 | 0.10 | 0.04 |
| 159.0 | 0.998±0.001 | 7.59 | 0.11 | 0.05 |
| 165.0 | 1.000±0.001 | 8.89 | 0.14 | 0.06 |
| 171.0 | 1.007±0.001 | 10.69 | 0.19 | 0.07 |
| 177.0 | 1.014±0.001 | 12.03 | 0.34 | 0.08 |

[a]This column lists point-to-point systematic uncertainties. In addition, there is an overall cross section scale uncertainty of ±1.5%.

Table II. We assign a systematic uncertainty to the correction factor for each angle bin, ranging from ±0.001 to ±10% of the correction itself, to allow for shortcomings in our approximation that the angle resolution profile can be adequately described by multiple Coulomb scattering through half the target thickness. Different recipes for numerical evaluation of the integrals in Eq. (11) provide answers consistent to better than this estimated uncertainty. We consider these smearing correction uncertainties to be uncorrelated from point to point. The correction factor is appreciably smaller than unity for the largest outgoing proton lab angle bins, because in these cases near the differential cross section minimum more events are multiply scattered into than out of the bin.

### E. Summary of angle dependence

The effect of the correction factors $c_i$ associated with the various sources of systematic error considered in this section is cumulative, and averages 1.10, with small variations with angle and data sample, as summarized in Table I. We assume, however, that the various uncertainties are uncorrelated with one another, and we add them in quadrature to obtain final systematic error estimates. The majority of error sources we have considered are explicitly or effectively angle independent; when combined, these yield an overall absolute normalization uncertainty of ±1.5%. The uncertainties associated with our measurements of acceptance and scattering angle (both systematic angle errors and angle resolution), and with trigger inefficiencies, are considered angle dependent and uncorrelated from point to point. These sources are combined to give the net point-to-point systematic uncertainties in Table II, where we also collect our final absolute cross section measurements obtained from a weighted average over the three independently analyzed and corrected data samples (1-punch, 2-stop with $E_{p1} \leqslant 5.0$ MeV, and 2-stop with $E_{p1} > 5.0$ MeV). The final cross sections differ very slightly from those reported in Ref. [21] because of the inclusion here of the multiple scattering correction indicated in Table II. The point-to-point and normalization uncertainties combine to give an overall systematic error of ±1.6% in most angle bins.

## VI. DISCUSSION

The preceding section provided a detailed catalog of the issues that must be carefully controlled to measure precise absolute cross sections with medium-energy neutron beams. To our knowledge, no previous experiments have attempted a comparable degree of control. The best existing absolute neutron-induced cross section standards at intermediate energies are from attenuation measurements of total cross sections [29], which are not suitable for calibrating neutron fluxes. It is hoped that the present results will provide a new calibration standard. The excellent agreement of our experimentally determined absolute cross section scale with that given by the Nijmegen PWA93 solution (see Fig. 14) confirms the consistency of our results with the total cross section measurements.

The level of agreement of our measurements with PWAs at $E_n = 194$ MeV is presented in more detail in Fig. 20. Here it is seen that, while the absolute cross section scale of the experimental results is in very good agreement with the Nijmegen PWA93 solution, there is a small systematic deviation in angular shape between the two: our results are higher than those of PWA93 by 2%–3% for $135 < \theta_{\text{c.m.}} < 165^\circ$ and lower by a similar amount for $100 < \theta_{\text{c.m.}} < 130^\circ$. These deviations considerably exceed our estimated

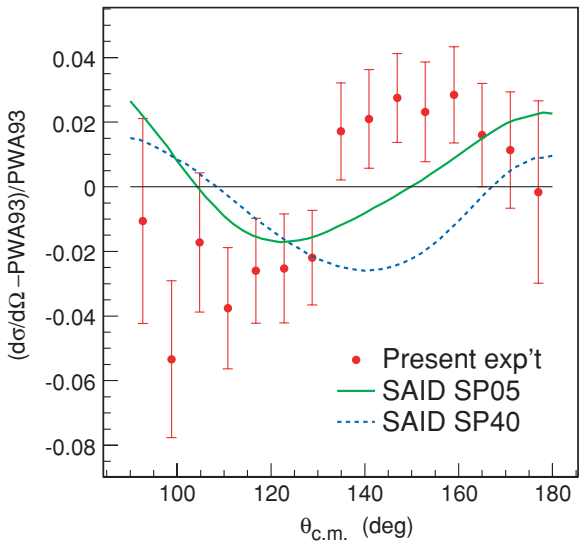


FIG. 20. (Color online) The relative differences of the present absolute *np* scattering differential cross sections and of two SAID PWA solutions [4,30] from the Nijmegen PWA93 solution [5,24], all at $E_n = 194$ MeV. The SP40 solution is from a 2003 analysis of the database from 0 – 400 MeV, while SP05 is the current SAID solution, fitted over the range 0–3.0 GeV, including the present data in the fit.

systematic uncertainty in the angle dependence. In particular, we note that the forward detector acceptance used in the former angle range is already essentially 100% (see Fig. 12), so that the extracted cross section cannot be overestimated by virtue of underestimating acceptance. Furthermore, the results for the three independently analyzed data samples agree extremely well in this angle region (see Fig. 13). We do see a possible small, statistically marginal, systematic deviation among our three data samples in Fig. 13 over the angle region from 100 to 130°, with the 1-punch cross sections falling on average a few percent below those for the two 2-stop event samples. However, even if this difference reflects a real systematic problem, it could only pull the averaged cross section down by less than 0.5% in this region, too small to account for the deviation from PWA93 in Fig. 20.

We also show in Fig. 20 the relative differential cross section differences between two recent SAID PWA solutions [4,30] and the Nijmegen PWA93. The various PWA solutions differ from one another by as much as 2%–3% also in the angle region displayed. Furthermore, we note that the SAID solution has shifted by ∼2% after inclusion of the present results in the fitted *np* database (even though that inclusion was carried out by adding our full, mostly angle-independent, systematic uncertainties in quadrature with our statistical uncertainties, thereby underweighting the present data in the fit). We conclude that the deviations between the present results and PWA93 are of the same order as the present uncertainties in the PWA solutions and most likely point to the need to refit phase shifts. We note, however, that there is a conceptual flaw in the procedures for such refitting to a database where all experiments have systematic uncertainties, but there is considerable variability in the level at which those systematic uncertainties are reported in the literature.

Finally, we address the comparison of the present results with those from the recent experiments by the Uppsala [7] and Freiburg [9] groups, both of which have been rejected from the *np* database used in the Nijmegen and SAID PWAs. As illustrated in Fig. 14 by the comparison of the two experimental results with PWA curves at the respective energies of the experiments, the present results deviate systematically from those of [7] in the steepness of the back-angle rise in cross section. These deviations are larger than the differences anticipated from the difference in neutron energy between the two experiments. There is a similar, though not quite as pronounced, systematic deviation of the present results from those of Franz *et al.* [9] shown in Fig. 1.

It is difficult to say definitively whether there might be a common problem that caused excessive cross sections near $\theta_{\mathrm{c.m.}} = 180^\circ$ in both of these earlier, completely independent and quite different, experiments [7,9]. We note only that measurements near $\theta_p^{\mathrm{sc}} = 0^\circ$, where the solid angle is vanishing, can be tricky with a secondary neutron beam of sizable angular divergence. One of the great advantages of the use of a tagged beam is that we are able in the present experiment to determine the neutron incidence angle event by event. Without such tagging information, the beam angular spread would contribute to the experimental angle resolution and thereby to migration of analyzed scattering events among proton lab angle bins. The bin migration effects in this case are more complicated than those treated in Sec. V D3, because only events that begin and end within the detector acceptance can now migrate. The acceptance for a spatially extended secondary beam depends on both incident and outgoing nucleon directions and on position of impact on the secondary target as well. In particular, the acceptance can be systematically different for the events most likely to migrate, because they preferentially populate outer regions in impact position on target, than for the events most likely to be retained within the same angle bin. Thus, the extracted cross section can suffer not only from averaging over a resolution function but also from acceptance evaluations that do not take proper account of the resolution smearing.

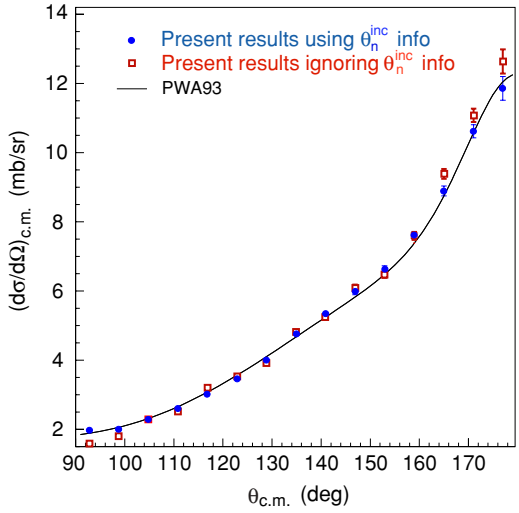


FIG. 21. (Color online) The effect on the present analysis of neglecting tagger information about the neutron incidence angle in the reconstruction of the *np* scattering angle for each event. The solid circles represent the final results (before multiple scattering corrections), while the open squares result when the scattering angle is estimated only with respect to the central neutron beam direction. Note the suppressed zero on the cross section scale.

We demonstrate these effects in Fig. 21 by comparing the present results with those we would have extracted had we chosen to ignore the neutron incidence angle information from the tagger in reconstructing the *np* scattering angle event by event. We thus bin the events in $\theta_p^{\mathrm{lab}}$ (measured with respect to the central neutron beam direction) rather than in $\theta_p^{\mathrm{sc}}$. In this alternative analysis, the yield per angle bin in the numerator of Eq. (1) is altered, whereas the solid angle and acceptance functions in the denominator are not. Such neglect is seen to give rise to a systematic overestimate of the cross section at the largest angles by ∼5% and to a substantial underestimate near $\theta_{\mathrm{c.m.}} = 90^\circ$. The latter effect (opposite in sign and much larger than the effect of multiple scattering smearing summarized in Table II) can be easily understood, because the acceptance of our detector array is plunging to zero forward of $\theta_{\mathrm{c.m.}} = 90^\circ$. Here, then, events can migrate out of an analyzed bin in either direction, but can effectively migrate into the bin only from $\theta_p^{\mathrm{sc}} < \theta_p^{\mathrm{lab}}$, strongly reducing the apparent yield without an appropriate compensation in the calculated acceptance.

Similarly, near $\theta_{\mathrm{c.m.}} = 180^\circ$ the vanishing solid angle implies that there are many more events that can migrate into a given $\theta_p^{\mathrm{lab}}$ bin from $\theta_p^{\mathrm{sc}} > \theta_p^{\mathrm{lab}}$ (induced by neutrons deviating from the central beam direction) than can migrate out of the bin. When the acceptance calculation does not account for these skewed origins, the result is an overestimated cross section. The effect would differ for different experiments, depending on the angular profile of the neutron beam, including any effects from scattering off collimator edges (the present experiment used no collimators), other contributions to the angle resolution, the angle bin size used in the analysis, and the detector acceptances and acceptance evaluation procedures. The experiments in Refs. [7,9] presumably had neutron incidence angle spreads that were substantially smaller (though not as well measured) than those of the present experiment, but they also utilized considerably finer angle binning. These two differences have competing influences on the sensitivity to the beam divergence, leaving the net effect in the earlier experiments unclear without more detailed information.

## VII. CONCLUSIONS

A tagged intermediate-energy neutron beam produced at the IUCF Cooler Ring has facilitated a measurement of the *np* scattering differential cross section at 194 MeV bombarding energy to an absolute precision $\approx \pm 1.5\%$ over the c.m. angular range 90°–180°. The usage of carefully matched and frequently interchanged solid $CH_2$ and C secondary targets permitted an accurate background subtraction, reducing reliance on kinematic cuts that might have introduced larger systematic uncertainties. The internal consistency in both magnitude and angular shape of the cross sections extracted from independent data samples characterized by substantially different neutron beam spatial and energy profiles supports the accuracy of the tagging technique. Systematic uncertainties in the measurement, affecting both the overall absolute scale of the cross sections and the angular dependence, have been carefully delineated, often via auxiliary measurements and analyses.

The present results are in reasonable agreement with the Nijmegen PWA93 calculation, over the full angular range covered, although there are systematic deviations at the 2%–3% level in the angular dependence that might be removed by minor tuning of phase shifts. In contrast, the present results deviate systematically from other recent measurements [7,9], especially in the steepness of the back-angle cross section rise. Our results thus appear to validate the omission of these earlier experiments from the database used in partial wave analyses of *np* elastic scattering, while also suggesting a conceivable experimental cause of the earlier overestimates of the cross section near $\theta_{\mathrm{c.m.}} = 180^\circ$. As the back-angle rise is particularly influential in pole extrapolations that have occasionally been used [12,13] to extract the charged pion-nucleon-nucleon coupling constant $f_c^2$, the present data also bear on that coupling strength. Since our measurements at the largest angles are consistent with, or even slightly less steep than, those of the PWA93 solution, a valid pole extrapolation analysis of the present results should yield a coupling constant value no larger than that ($f_c^2 = 0.0748 \pm 0.0003$) extracted from the Nijmegen PWA [6].

## ACKNOWLEDGMENTS

We thank the operations staff of the Indiana University Cyclotron Facility for providing the superior quality cooled beams and Hal Spinka and Catherine Lechanoine-Leluc for the loan of critical detector hardware needed for the successful execution of this experiment. We acknowledge the U.S. National Science Foundation's support under Grant Numbers NSF-PHY-9602872, 0100348, and 0457219.

[1] R. Machleidt and I. Slaus, J. Phys. G **27**, R69 (2001).
[2] D. R. Entem and R. Machleidt, Phys. Rev. C **68**, 041001(R) (2003).
[3] S. C. Pieper and R. B. Wiringa, Annu. Rev. Nucl. Part. Sci. **51**, 53 (2001); P. Navratil and E. W. Ormand, Phys. Rev. C **68**, 034305 (2003).
[4] http://lux2.phys.va.gwu.edu/analysis/nn_analysis.html
[5] V. G. J. Stoks, R. A. M. Klomp, M. C. M. Rentmeester, and J. J. deSwart, Phys. Rev. C **48**, 792 (1993).
[6] M. C. M. Rentmeester, R. G. E. Timmermans, and J. J. deSwart, Phys. Rev. C **64**, 034004 (2001).
[7] J. Rahm *et al.*, Phys. Rev. C **57**, 1077 (1998).
[8] W. Hürster *et al.*, Phys. Lett. **B90**, 367 (1980).
[9] J. Franz *et al.*, Phys. Scr. **T87**, 14 (2000).
[10] B. E. Bonner, J. E. Simmons, C. L. Hollas, C. R. Newsom, P. J. Riley, G. Glass, and M. Jain, Phys. Rev. Lett. **41**, 1200 (1978).
[11] D. V. Bugg and R. Machleidt, Phys. Rev. C **52**, 1203 (1995).
[12] T. E. O. Ericson *et al.*, Phys. Rev. Lett. **75**, 1046 (1995).
[13] *Proceedings of Workshop on Critical Issues in the Determination of the Pion-Nucleon Coupling Constant*, edited by J. Blomgren, Phys. Scr. **T87**, 33 (2000).
[14] M. C. M. Rentmeester, R. A. M. Klomp, and J. J. deSwart, Phys. Rev. Lett. **81**, 5253 (1998).
[15] T. E. O. Ericson *et al.*, Phys. Rev. Lett. **81**, 5254 (1998).
[16] R. A. Arndt, I. I. Strakovsky, and R. L. Workman, Phys. Rev. C **52**, 2246 (1995).
[17] T. Peterson *et al.*, Nucl. Instrum. Methods A **527**, 432 (2004).
[18] S. E. Vigdor, W. W. Jacobs, L. D. Knutson, J. Sowinski, C. Bloch, P. L. Jolivette, S. W. Wissink, R. C. Byrd, and C. Whiddon, Phys. Rev. C **46**, 410 (1992).
[19] J. Sowinski *et al.*, Phys. Lett. **199B**, 341 (1987).
[20] T. W. Bowyer, Ph.D. dissertation, Indiana University (1994, unpublished).
[21] M. Sarsour *et al.*, Phys. Rev. Lett. **94**, 082303 (2005).
[22] R. E. Pollock, Annu. Rev. Nucl. Part. Sci. **41**, 357 (1991).
[23] A. Ahmidouch *et al.*, Nucl. Instrum. Methods Phys. Res., Sec. A **326**, 538 (1993).
[24] http://nn-online.sci.kun.nl/NN/
[25] R. K. Tripathi, J. W. Wilson, and F. A. Cucinotta, NASA Technical Paper 3656 (1997) (http://hdl.handle.net/2002/13366).
[26] E. J. Stephenson *et al.*, Phys. Rev. Lett. **91**, 142302 (2003).

[27] H. A. Bethe, Phys. Rev. **89**, 1256 (1953).
[28] V. L. Highland, Nucl. Instrum. Methods **129**, 497 (1975); **161**, 171 (1979); G. R. Lynch and O. I. Dahl, Nucl. Instrum. Methods B **58**, 6 (1991).
[29] P. W. Lisowski, R. E. Shamu, G. F. Auchampaugh, N. S. P. King, M. S. Moore, G. L. Morgan, and T. S. Singleton, Phys. Rev. Lett. **49**, 255 (1982); V. Grundies, J. Franz, E. Rossle, and H. Schmitt, Phys. Lett. **B158**, 15 (1985); W. P. Abfalterer, F. B. Bateman, F. S. Dietrich, R. W. Finlay, R. C. Haight, and G. L. Morgan, Phys. Rev. C **63**, 044608 (2001).
[30] R. A. Arndt, I. I. Strakovsky, and R. L. Workman, Phys. Rev. C **62**, 034005 (2000).